CCD Photometry, Light Curve Modeling, and Period Study of Four Overcontact Binary Systems: EI CMi, NSVS 3092802, V1309 Her, and V958 Mon

Kevin B. Alton
UnderOak Observatory, 70 Summit Avenue, Cedar Knolls, NJ 07927; kbalton@optonline.net

Received July 20, 2020; revised October 2, 2020; accepted October 14, 2020

Abstract Precise time-series multi-color light curve data were acquired at Desert Blooms Observatory (DBO) from EI CMi (2018–2019), NSVS 3092802 (2018–2019), V958 Mon (2018), and V1309 Her (2018). Except for V958 Mon, only monochromatic CCD photometric data are available from automated surveys which employ sparse sampling strategies. Each target produced new times of minimum from data acquired at DBO which along with other eclipse timings from the literature and those extrapolated from various sources were used to generate new ephemerides. Secular analyses (eclipse timing differences vs. epoch) revealed changes in the orbital period of each system; related evidence suggests that V1309 Her may be a ternary system. Simultaneous modeling of multicolor light curve data from each target was accomplished using the Wilson-Devinney code. Each system exhibits a total eclipse, therefore a unique photometrically derived value for the mass ratio (q_{ptm}) could be determined which subsequently provided initial estimates for the physical and geometric elements of each variable system.

1. Introduction

Overcontact binaries (OCBs), also known as EW or W UMa-type variables, share a common atmosphere with varying degrees of physical contact. Light curves (LCs) typically exhibit eclipse minima with near equal depth that reveal little color change, thereby suggesting they have similar surface temperatures. Assuming that one defines the most massive as the primary star, as is the case herein, the majority of OCBs have mass ratios ($q = m_2 / m_1$) that range from unity to as low as 0.065–0.08 (Sriram *et al.* 2016; Mochnacki and Doughty 1972; Paczyński *et al.* 2007; Arbutina 2009). For the most part, their evolutionary lifetimes are spent in physical contact (Stępień 2006; Gazeas and Stępień 2008; Stępień and Kiraga 2015). Furthermore, depending on many factors, including rate of angular momentum loss, mass ratio, total mass, orbital period, and metallicity, OCBs are destined to coalesce into fast rotating stars or to alternatively produce exotic objects such as blue stragglers (Qian *et al.* 2006; Stępień and Kiraga 2015), double degenerate binaries, supernovae, or even double black holes (Almeida *et al.* 2015).

The latest estimates appearing on the NASA Chandra website (https://chandra.harvard.edu/xray_sources/binary_stars.html) suggest that over 80% of all stars are in some arrangement of two or more gravitationally bound partners. Advances in detector technology and algorithms to reliably classify variable stars from large data sets have not only led to significantly increased density of eclipsing binaries (EBs) detected in a given survey field but an improvement in the statistical estimates for the prevalence of OCBs. Early estimates (van't Veer 1975) suggested that 1/500 stars in the study sample (GCVS; Kukarkin *et al.* 1970) was a contact binary (CB), while later on Ruciński (1994) projected that the incidence of CBs found amongst F-K type main sequence stars located in older clusters was somewhat greater 1/250–300. The microlensing technique advanced by the OGLE Survey (Udalski *et al.* 1992) produced a rich source of low amplitude EBs that would have otherwise gone undetected. Nearly two-thirds of the 931 eclipsing binaries detected during this study were classified as contact binaries (Ruciński 1997a, 1997b). Classification of 11,099 EBs detected in the ASAS study (Paczyński *et al.* 2006) revealed that 48.6% were OCBs, while Christiansen *et al.* (2008) found a slightly larger proportion (56.9%) amongst all detected EBs in a University of New South Wales Survey. Prša *et al.* (2011) reported a 1.5-fold increase in the occurrence rate of EB stars found in the Kepler field (1.2%) as opposed to the earlier Hipparcos survey (0.8%). In the Kepler field-of-view (FOV), 25.4% of the manually classified EBs were determined to be OCBs, which translates into 1 OCB per 328 target stars. Differences in the demographic breakdown of OCBs as a fraction of total eclipsing binaries clearly depends on the survey catalog, selection criteria, galactic latitude, or cluster age. Nonetheless, far from being a rare type of eclipsing variable, OCBs in some cases have been shown to represent over 50% of the total population of EBs found in a study sample.

Aside from a comprehensive (V, g', i', and r') study of V958 Mon published by Michaels (2016), no other multi-color light curves with Roche modeling have been reported for any of the other binary systems described herein. As a result, this investigation also provides the first published photometric mass ratio (q_{ptm}) estimates along with preliminary physical and geometric characteristics for NSVS 3092802, V1309 Her, and EI CMi.

2. Observations and data reduction

Time-series images were acquired at Desert Blooms Observatory (DBO, USA, 31.941 N, 110.257 W) with an SBIG STT-1603ME CCD camera mounted at the Cassegrain focus of a 0.4-m Schmidt-Cassegrain telescope. This focal-reduced (f/6.8) instrument produces an image scale of 1.36 arcsec/pixel (bin = 2 × 2) and a field-of-view (FOV) of 17.2 × 11.5 arcmin. Image acquisition was performed using TheSkyX professional edition 10.5.0 (Software Bisque 2019). Computer time was

updated immediately prior to each session and exposure time for all images adjusted to 75 s. The CCD camera is equipped with B, V, R_c, and I_c filters manufactured to match the Johnson-Cousins Bessell specification. Dark subtraction, flat correction, and registration of all images collected at DBO were performed with AIP4WIN v2.4.0 (Berry and Burnell 2005). Instrumental readings from V1309 Her and V958 Mon were reduced to catalog-based magnitudes using APASS DR9 values (Henden *et al.* 2009, 2010, 2011; Smith *et al.* 2011), whereas the MPOSC3 star fields (Warner 2007) built into MPO CANOPUS v 10.7.1.3 (Minor Planet Observer 2010) were used for EI CMi and NSVS 3092802.

3. Results and discussion

Light curves were generated using an ensemble of at least four non-varying comparison stars. The identity, J2000 coordinates, and color indices (*B–V*) for these stars are provided in Table 1. Only data from images taken above 30° altitude (airmass < 2.0) were included; considering the proximity of all program stars, differential atmospheric extinction was ignored. Uncertainty in comparison star measurements made in the same FOV typically stayed within ± 0.007 mag for V-, I_c-, and R_c-, and ± 0.010 mag for B-passbands. CCD images annotated with the location of target and comparison stars are shown for EI CMi (Figure 1), NSVS 3092802 (Figure 2), V958 Mon (Figure 3), and V1309 Her (Figure 4). All photometric data can be retrieved from the AAVSO International Database via the International Variable Star Index (Watson *et al.* 2014; https://www.aavso.org/data-download).

3.1. Photometry and ephemerides

Times-of-minimum (ToM) and associated errors were calculated using the method of Kwee and van Woerden (1956) as implemented in PERANSO v2.5 (Paunzen and Vanmunster 2016). Curve fitting all eclipse timing differences (ETD) was accomplished using scaled Levenberg-Marquardt algorithms (QTIPLOT 0.9.9-rc9; IONDEV SRL 2020). The acquisition dates and number of data points for each bandpass used for the determination of ToM values and/or Roche modeling are summarized in Table 2. The results from these analyses are separately discussed for each binary system in the subsections below.

3.1.1 EI CMi

EI CMi was initially detected in the calibration fields for the Sloan Digital Sky Survey (Henden and Stone 1998) and confirmed to be an EW binary by Greaves and Wils (2003). Later on (2001–2009) EI CMi was also captured by the All Sky Automated Survey (ASAS, Pojmański *et al.* 2005). When period folded by ANOVA (Paunzen and Vanmunster 2016), LC data from ASAS yielded an orbital period of 0.362536 ± 0.000006 d.

Fifteen new ToM measurements (5 / bandpass) were extracted from photometric data acquired at DBO. These along with seven other eclipse timings found in the literature (Table 3) were used to calculate a new linear ephemeris (Equation 1) based on near term data produced between 2014 and 2020:

$$\text{Min.I (HJD)} = 2458899.4685\,(3) + 0.36253496\,(13)\,\text{E} \quad (1)$$

Table 1. Astrometric coordinates (J2000), V-magnitudes and color indices (B–V) for EI CMi (Figure 1), NSVS 3092802 (Figure 2), V958 Mon (Figure 3), and V1309 Her (Figure 4) with their corresponding comparison stars used in this photometric study.

Star Identification	*R.A. (J2000)* h m s	*Dec. (J2000)* ° ′ ″	*V mag.*	*(B–V)*
(T) EI CMi[a]	07 57 06.278	+01 17 19.91	13.239	0.645
(1) GSC 00180-1688	07 50 09.835	+00 45 52.16	12.250	0.508
(2) GSC 00180-1188	07 47 48.722	+00 12 53.28	11.931	0.716
(3) GSC 00180-1176	07 45 08.287	+00 34 16.39	13.077	0.430
(4) GSC 00180-2269	07 51 52.498	+00 39 38.05	12.854	0.521
(5) GSC 00180-2280	07 51 24.298	+00 05 05.82	12.664	0.491
(T) NSVS 3092802[a]	19 47 22.495	+53 52 34.32	13.075	0.830
(1) GSC 03935-0749	19 47 33.233	+53 55 40.76	11.735	0.708
(2) GSC 03935-0605	19 47 25.318	+53 54 42.77	12.992	0.751
(3) GSC 03935-0365	19 46 49.236	+53 52 21.11	12.043	0.641
(4) GSC 03935-0885	19 46 44.561	+53 50 37.97	12.623	0.751
(5) GSC 03935-1077	19 46 58.442	+53 45 45.18	11.760	0.614
(T) V958 Mon[b]	06 22 06.393	+04 28 16.47	11.976	0.844
(1) GSC 00140-1092	06 21 28.259	+04 22 59.44	12.750	0.534
(2) GSC 00140-0803	06 21 55.665	+04 26 50.65	13.305	0.553
(3) GSC 00140-1189	06 21 56.880	+04 27 05.92	12.794	0.602
(4) GSC 00140-0335	06 21 28.259	+04 22 59.44	13.434	0.600
(5) GSC 00140-1059	06 22 06.121	+04 29 51.18	12.549	1.372
(T) V1309 Her[b]	17 55 35.842	+43 48 20.15	12.123	0.560
(2) GSC 03101-1293	17 55 23.098	+43 54 29.38	11.329	0.677
(3) GSC 03101-1051	17 54 45.406	+43 51 10.62	13.237	0.785
(4) GSC 03101-1288	17 54 47.784	+43 50 36.64	13.023	0.760
(5) GSC 03101-1624	17 55 27.878	+43 49 06.49	13.394	0.718

[a] V-mag and (B–V) for comparison stars derived from MPOSC3 database described by Warner (2007). [b] V-mag and (B–V) for comparison stars derived from APASS DR9 database described by Henden et al. *(2009, 2010, 2011) and Smith* et al. *(2011).*

When all ToM data were included (2002–2019), plotting (Figure 5) the difference between observed eclipse times and those predicted by the linear ephemeris against epoch (cycle number) reveals what appears to be a quadratic relationship (Equation 2) where:

$$\text{ETD} = -4.658 \pm 5.07 \cdot 10^{-4} - 5.715 \pm 2.503 \cdot 10^{-7}\,\text{E} - 1.054 \pm 0.147 \cdot 10^{-10}\,\text{E}^2. \quad (2)$$

In this case the ETD residuals vs. epoch can be described by a second order polynomial with a negative quadratic coefficient ($-1.054 \cdot 10^{-10}$), suggesting that the orbital period has been slowly decreasing over time at the rate of 0.0184 (26) $s \cdot y^{-1}$. A secular period change associated with an ETD diagram described by a parabola is often attributed to mass transfer or by angular momentum loss (AML) due to magnetic stellar wind. Ideally, when AML dominates, the net effect is a decreasing orbital period. If conservative mass transfer from the primary to a secondary star prevails, then the orbital period can also speed up. The separation increases when conservative mass transfer from the less massive to a more massive component takes place or spherically symmetric mass loss from either body (e.g. a wind but not magnetized) occurs. In mixed situations (e.g. mass transfer from less massive star, together with AML) the orbit evolution depends on which process prevails. It should

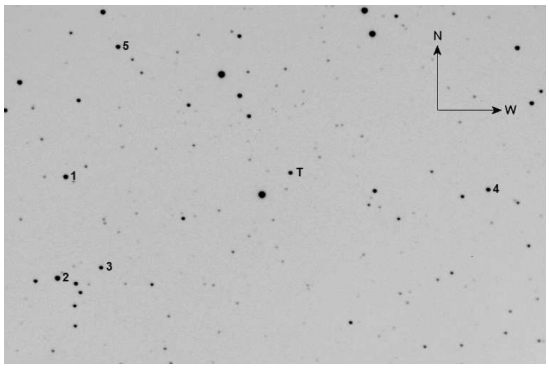

Figure 1. CCD image (V-mag) of EI CMi (T) showing the location of comparison stars (1–5) used to generate MPOSC3-derived magnitude estimates. The FOV for all OCBs reported herein is 17.2 × 11.5 arcmin.

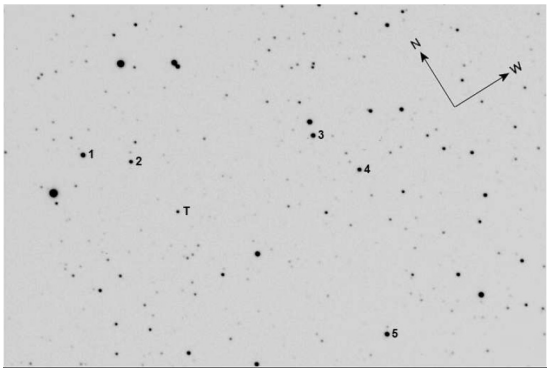

Figure 2. CCD image (V-mag) of NSVS 3092802 (T) showing the location of comparison stars (1–5) used to generate MPOSC3-derived magnitude estimates.

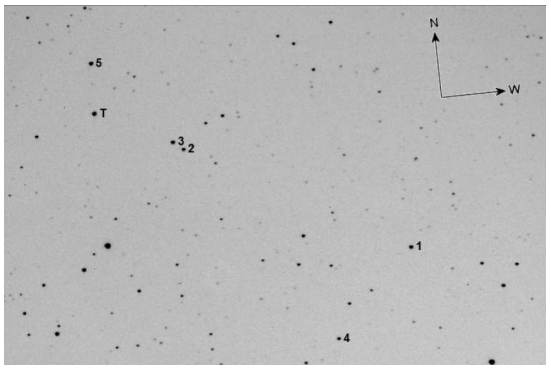

Figure 3. CCD image (V-mag) of V958 Mon (T) showing the location of comparison stars (1–5) used to generate APASS-derived magnitude estimates.

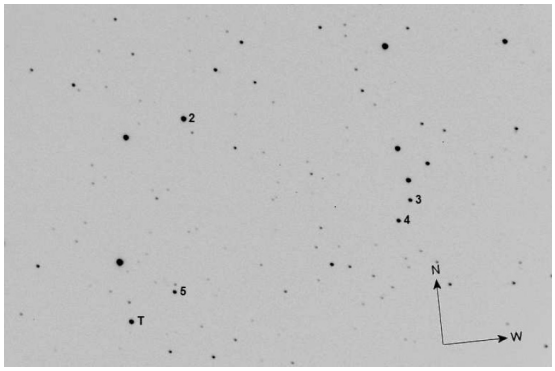

Figure 4. CCD image (V-mag) of V1309 Her (T) showing the location of comparison stars (2–5) used to generate APASS-derived magnitude estimates.

Table 2. Chronicle of image acquisition dates and number of data points in each bandpass (BVI_cR_c) used for the determination of ToM values and/or Roche modeling.

Target Identification	*B*	*V*	I_c	R_c	*Dates*
EI CMi	425	428	438	—	December 21, 2018–February 7, 2019
NVSV 3092802	612	634	619	—	September 22, 2018–June 3, 2019
V958 Mon[a]	289	304	297	—	January 31, 2018–February 4, 2018
V958 Mon	271	295	277	295	November 27, 2018–December 12, 2018
V1309 Her	413	381	424	—	June 21, 2018–June 25, 2018

[a] *LCs incomplete only used for determination of ToM values.*

Table 3. EI CMi times-of-minimum (April 25, 2002–February 7, 2019), cycle number and residuals (ETD) between observed and predicted times derived from the updated linear ephemeris (Equation 1).

HJD 2400000+	*HJD Error*	*Cycle No.*	*ETD*[a]	*Reference*
52390.49000	nr	–17954	–0.02582	1
53478.47100	nr	–14953	–0.01224	2
55564.86480	0.00030	–9198	–0.00714	2
56726.43420	0.00170	–5994	0.00024	3
56968.60670	0.00020	–5326	–0.00061	4
57013.56200	0.00200	–5202	0.00036	5
58473.85137	0.00023	–1174	–0.00110	6
58473.85231	0.00017	–1174	–0.00015	6
58473.85325	0.00020	–1174	0.00078	6
58475.84528	0.00033	–1168.5	–0.00113	6
58475.84560	0.00025	–1168.5	–0.00081	6
58475.84777	0.00037	–1168.5	0.00136	6
58479.83289	0.00030	–1157.5	–0.00141	6
58479.83393	0.00011	–1157.5	–0.00036	6
58479.83490	0.00027	–1157.5	0.00060	6
58487.80863	0.00033	–1135.5	–0.00143	6
58487.81033	0.00016	–1135.5	0.00027	6
58487.81096	0.00025	–1135.5	0.00089	6
58521.70709	0.00010	–1042	0.00001	6
58521.70799	0.00024	–1042	0.00091	6
58521.70890	0.00030	–1042	0.00182	6
58899.46830	0.00010	0	–0.00021	7

[a] *ETD = Eclipse Time Difference.* [b] *nr = Not reported.*
References: 1. Greaves and Wils (2003); 2. Diethelm (2011); 3. Hübscher and Lehmann (2015); 4. Juryšek et al. *(2017); 5. Paschke (2015); 6. This study at DBO; 7. Paschke (2020).*

be noted that only six eclipse timings for EI CMi are available before 2018. Nonetheless, the apparent quadratic fit of the ETD residuals (Figure 5), would suggest a secular change in the orbital period similar to many other contact systems reported in the literature (Giménez *et al.* 2006). Given the paucity of data, no other underlying variations in the orbital period stand out such as those that might be caused by magnetic cycles (Applegate 1992) or the presence of an additional gravitationally bound stellar-sized body. At a minimum, another decade of precise times of minimum will still be needed to confirm whether the orbital period of this system is truly changing in a predictable fashion.

3.1.2. NSVS 3092802

Broad band (450–1000 nm) monochromatic CCD-derived photometric data for this system were first obtained from the ROTSE-I survey between 1999 and 2000 (Akerlof *et al.* 2000;

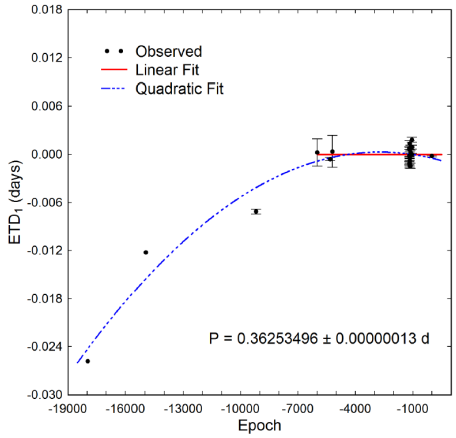

Figure 5. Eclipse timing differences (ETD) vs. epoch for EI CMi calculated using the updated linear ephemeris (Equation 1). When available, measurement uncertainty is denoted by the hatched vertical lines. The dashed blue line represents the quadratic fit while the solid red line within the figure insert indicates the linear fit.

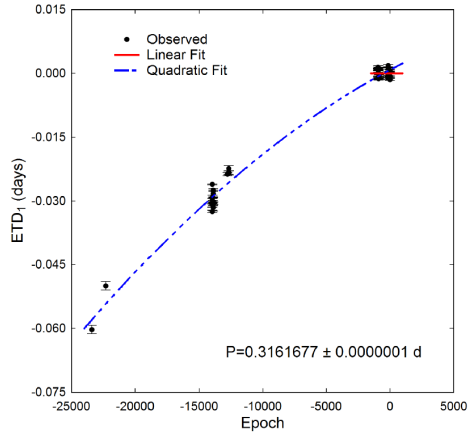

Figure 6. Eclipse timing differences (ETD) vs. epoch for NSVS 3092802 calculated using the updated linear ephemeris (Equation 3). Measurement uncertainty is denoted by the hatched vertical lines. The solid red line within the figure illustrates the linear fit while the blue dashed line represents the quadratic fit (Equation 4) from all data.

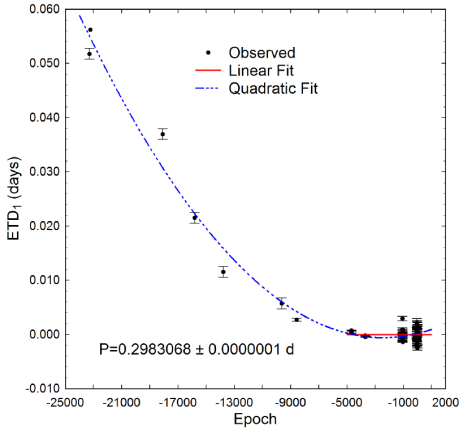

Figure 7. Eclipse timing differences (ETD) vs. epoch for V958 Mon calculated using the updated linear ephemeris (Equation 5). Measurement uncertainty is denoted by the hatched vertical lines. The solid red line within the figure indicates the linear fit while the blue dashed line represents the quadratic fit (Equation 6) from all data.

Table 4. NSVS 3092802 times-of-minimum (April 20, 1999–July 20, 2019), cycle number and residuals (ETD) between observed and predicted times derived from the updated linear ephemeris (Equation 3).

HJD 2400000+	*HJD Error*	*Cycle No.*	*ETD*[a]	*Ref.*
51288.83150	0.0010	–23392	–0.06025	1
51630.77720	0.0010	–22310.5	–0.04997	1
54261.62850	0.0002	–13989.5	–0.03050	2
54265.58132	0.0004	–13977	–0.02977	2
54266.53348	0.0001	–13974	–0.02612	2
54267.63531	0.0006	–13970.5	–0.03088	2
54270.63727	0.0003	–13961	–0.03250	2
54277.59640	0.0004	–13939	–0.02907	2
54279.65005	0.0006	–13932.5	–0.03051	2
54288.50580	0.0004	–13904.5	–0.02745	2
54290.55753	0.0003	–13898	–0.03081	2
54291.50600	0.0003	–13895	–0.03085	2
54291.66478	0.0009	–13894.5	–0.03015	2
54292.61189	0.0008	–13891.5	–0.03155	2
54293.56367	0.0008	–13888.5	–0.02827	2
54295.61650	0.0003	–13882	–0.03053	2
54645.62100	0.0004	–12775	–0.02373	2
54663.48481	0.0004	–12718.5	–0.02339	2
54670.59962	0.0006	–12696	–0.02236	2
54684.50996	0.0005	–12652	–0.02340	2
58383.69494	0.0003	–952	–0.00107	3
58383.69685	0.0002	–952	0.00084	3
58383.69744	0.0003	–952	0.00143	3
58389.70235	0.0002	–933	–0.00085	3
58389.70339	0.0001	–933	0.00020	3
58389.70431	0.0002	–933	0.00111	3
58396.65790	0.0003	–911	–0.00099	3
58396.65904	0.0000	–911	0.00015	3
58396.65993	0.0002	–911	0.00104	3
58398.71274	0.0004	–904.5	–0.00124	3
58398.71286	0.0004	–904.5	–0.00112	3
58398.71521	0.0006	–904.5	0.00123	3
58401.71667	0.0003	–895	–0.00091	3
58401.71757	0.0000	–895	0	3
58401.71864	0.0003	–895	0.00107	3
58411.67596	0.0003	–863.5	–0.00089	3
58411.67635	0.0002	–863.5	–0.00051	3
58411.67671	0.0002	–863.5	–0.00014	3
58632.83577	0.0006	–164	–0.00043	3
58632.83591	0.0007	–164	–0.00028	3
58634.89022	0.0004	–157.5	–0.00106	3
58634.89239	0.0002	–157.5	0.00111	3
58634.89302	0.0004	–157.5	0.00173	3
58637.89387	0.0005	–148	–0.00101	3
58637.89603	0.0002	–148	0.00115	3
58637.89667	0.0003	–148	0.00179	3
58663.66249	0.0001	–66.5	–0.00006	4
58663.82083	0.0002	–66	0.0002	4
58680.73610	0.0002	–12.5	0.00049	4
58681.84148	0.0000	–9	–0.00072	4
58682.79091	0.0003	–6	0.00021	4
58683.73774	0.0002	–3	–0.00147	4
58683.89634	0.0001	–2.5	–0.00095	4
58684.68702	0.0001	0	–0.00068	4
58684.84642	0.0002	0.5	0.00063	4

[a] *ETD = Eclipse Time Difference. References: 1. NSVS; 2. SuperWASP; 3. This study at DBO; 4. The International Variable Star Index.*
This table is available through the AAVSO ftp site at

ftp://ftp.aavso.org/public/datasets/Alton-eicmi-tab4.txt

(if necessary, copy and paste link into the address bar of a web browser).

Table 5. V958 Mon times-of-minimum (December 3, 1999–December 12, 2018), cycle number and residuals (ETD) between observed and predicted times derived from the updated linear ephemeris (Equation 5).

HJD 2400000+	HJD Error	Cycle No.	ETD[a]	Ref.	HJD 2400000+	HJD Error	Cycle No.	ETD[a]	Ref.
51515.9100	0.0010	–23294.5	0.05175	1	58451.7891	0.0005	–43.5	–0.00105	7
51525.8910[b]	nr[c]	–23261	0.03948	2	58451.7901	0.0002	–43.5	–0.00008	7
51535.9010	0.0010	–23227.5	0.05620	1	58451.7906	0.0005	–43.5	0.00043	7
53068.5822	0.0010	–18089.5	0.03694	3	58451.7912	0.0003	–43.5	0.00096	7
53744.6792	0.0010	–15823	0.02152	3	58451.7921	0.0007	–43.5	0.00188	7
54355.8999	0.0010	–13774	0.01154	3	58451.9376	0.0006	–43	–0.00172	7
55588.6470	0.0003	–9641.5	0.00570	4	58451.9392	0.0015	–43	–0.00015	7
55907.8323	0.0003	–8571.5	0.00270	5	58451.9393	0.0009	–43	–0.00007	7
57065.7080	0.0001	–4690	0.00046	6	58451.9396	0.0002	–43	0.00026	7
57066.6032	0.0001	–4687	0.00074	6	58451.9407	0.0005	–43	0.00133	7
57071.6742	0.0001	–4670	0.00053	6	58455.8150	0.0010	–30	–0.00231	7
57359.8379	0.0001	–3704	–0.00017	6	58455.8160	0.0006	–30	–0.00129	7
57360.7327	0.0002	–3701	–0.00029	6	58455.8163	0.0010	–30	–0.00104	7
57361.7766	0.0002	–3697.5	–0.00046	6	58455.8169	0.0017	–30	–0.00043	7
57362.8209	0.0002	–3694	–0.00023	6	58455.8172	0.0001	–30	–0.00014	7
57363.7158	0.0002	–3691	–0.00025	6	58455.9664	0.0014	–29.5	–0.00004	7
58149.6041	0.0004	–1056.5	–0.00132	7	58455.9675	0.0010	–29.5	0.00102	7
58149.6051	0.0001	–1056.5	–0.00027	7	58455.9677	0.0008	–29.5	0.00120	7
58149.6083	0.0007	–1056.5	0.00292	7	58455.9684	0.0008	–29.5	0.00190	7
58149.7535	0.0003	–1056	–0.00105	7	58456.8606	0.0006	–26.5	–0.00085	7
58149.7540	0.0001	–1056	–0.00053	7	58456.8616	0.0001	–26.5	0.00018	7
58149.7545	0.0002	–1056	–0.00002	7	58456.8621	0.0007	–26.5	0.00067	7
58150.6482	0.0003	–1053	–0.00126	7	58456.8626	0.0004	–26.5	0.00117	7
58150.6490	0.0001	–1053	–0.00041	7	58456.8636	0.0011	–26.5	0.00218	7
58150.6500	0.0003	–1053	0.00054	7	58461.7809	0.0011	–10	–0.00252	7
58150.7974	0.0003	–1052.5	–0.00116	7	58461.7821	0.0008	–10	–0.00136	7
58150.7986	0.0001	–1052.5	–0.00003	7	58461.7832	0.0008	–10	–0.00030	7
58150.7996	0.0004	–1052.5	0.00095	7	58461.7843	0.0003	–10	0.00087	7
58151.6922	0.0003	–1049.5	–0.00138	7	58461.7853	0.0008	–10	0.00179	7
58151.6932	0.0001	–1049.5	–0.00034	7	58464.7643	0.0009	0	–0.00224	7
58151.6942	0.0003	–1049.5	0.00069	7	58464.7656	0.0004	0	–0.00098	7
58153.7810	0.0001	–1042.5	–0.00071	7	58464.7661	0.0006	0	–0.00048	7
58153.7815	0.0001	–1042.5	–0.00020	7	58464.7667	0.0002	0	0.00014	7
58153.7822	0.0002	–1042.5	0.00051	7	58464.7677	0.0006	0	0.00115	7
58161.6866	0.0001	–1016	–0.00017	8	58464.9160	0.0013	0.5	0.00030	7
58449.9996	0.0004	–49.5	–0.00077	7	58464.9162	0.0002	0.5	0.00051	7
58450.0002	0.0010	–49.5	–0.00015	7	58464.9165	0.0009	0.5	0.00082	7
58450.0004	0.0012	–49.5	0.00005	7	58464.9173	0.0007	0.5	0.00166	7
58450.0006	0.0012	–49.5	0.00026	7					

[a] *ETD = Eclipse Time Difference.* [b] *Outlier.* [c] *Not reported. References: 1. NSVS; 2. Otero* et al. *(2004); 3. ASAS; 4. Diethelm (2011); 5. Nelson (2012); 6. Michaels (2016); 7. This study at DBO; 8. The International Variable Star Index.*
This table is available through the AAVSO ftp site at ftp://ftp.aavso.org/public/datasets/Alton-eicmi-tab5.txt (if necessary, copy and paste link into the address bar of a web browser).

Gettel *et al.* 2006) and thereafter classified as a WUMa-type variable according to Hoffman *et al.* 2009. These data are maintained in the Northern Sky Variability Survey (NSVS; Woźniak *et al.* 2004) archives (https://skydot.lanl.gov/nsvs/nsvs.php). NSVS 3092802 was also imaged during the SuperWASP survey (Butters *et al.* 2010) which provided a rich source of photometric data taken (30-s exposures) at modest cadence that repeats every 9 to 12 min. In some cases (18) SuperWASP measurements taken between 2007 and 2008 were amenable to further analysis using the method of Kwee and van Woerden (1956) to estimate ToM values. Light curve data (BVI_c) acquired at DBO produced 26 new ToM values. These results along with other eclipse timings (Table 4) derived from the NSVS archives, SuperWASP, and the International Variable Star Index were used to calculate a new linear ephemeris (Equation 3) based on near-term data (2018–2019):

$$\text{Min.I (HJD)} = 2458684.6877\,(3) + 0.3161677\,(4)\,\text{E}. \quad (3)$$

When all ToM data were included (1999–2019), a quadratic relationship (Equation 4) was established after plotting (Figure 6) the difference between the observed eclipse times and those predicted by the linear ephemeris against epoch whereby:

$$\text{ETD} = 8.01 \pm 3.06 \cdot 10^{-4} + 1.59 \pm 0.12 \cdot 10^{-6}\,\text{E} - 3.93 \pm 0.66 \cdot 10^{-11}\,\text{E}^2. \quad (4)$$

In this case the ETD residuals vs. epoch suggest that the orbital period has been very slowly decreasing ($-0.008\,(1)\,\text{s} \cdot \text{y}^{-1}$), based on the negative quadratic coefficient ($-3.93\,(66) \cdot 10^{-11}$).

3.1.3. V958 Mon

Monochromatic photometric data for V958 Mon were first obtained from the ROTSE-I survey between 1999 and 2000 (Akerlof *et al.* 2000; Woźniak *et al.* 2004; Gettel *et al.* 2006) and classified later as a W UMa-type variable (Hoffman *et al.* 2009).

Table 6. V1309 Her times-of-minimum (June 29, 1999–June 25, 2018), cycle number and residuals (ETD) between observed and predicted times derived from the updated linear ephemeris (Equation 7).

HJD 2400000+	*HJD Error*	*Cycle No.*	*ETD*[a]	*Ref.*	*HJD 2400000+*	*HJD Error*	*Cycle No.*	*ETD*[a]	*Ref.*
51358.6965	0.0008	–18752	0.03764	1	54628.6353	0.0002	–9911.5	0.01117	2
51364.7978	0.0009	–18735.5	0.03585	1	54639.5444	0.0005	–9882	0.00868	2
53121.5467	0.0005	–13986	0.01760	1	54643.4312	0.0004	–9871.5	0.01166	2
53143.3703	0.0019	–13927	0.01800	1	54650.4557	0.0002	–9852.5	0.00842	2
53150.3981	0.0006	–13908	0.01800	1	54651.5686	0.0003	–9849.5	0.01162	2
53150.5821	0.0015	–13907.5	0.01705	1	54652.4907	0.0003	–9847	0.00908	2
53152.6185	0.0003	–13902	0.01904	2	54656.5613	0.0002	–9836	0.01091	2
53154.4662	0.0005	–13897	0.01736	1	54670.4290	0.0003	–9798.5	0.00792	2
53154.6557	0.0004	–13896.5	0.02190	2	54674.5005	0.0003	–9787.5	0.01065	2
53162.6047	0.0003	–13875	0.01840	2	54675.4226	0.0004	–9785	0.00804	2
53163.5308	0.0006	–13872.5	0.01983	2	54681.5281	0.0004	–9768.5	0.01049	2
53169.6355	0.0002	–13856	0.02139	2	54682.4520	0.0002	–9766	0.00964	2
53171.6701	0.0002	–13850.5	0.02166	2	54684.4864	0.0005	–9760.5	0.00975	2
53172.5934	0.0003	–13848	0.02024	2	54919.9164	0.0003	–9124	0.00808	6
53173.5150	0.0003	–13845.5	0.01710	1	55067.4980	0.0008	–8725	0.00575	7
53177.5864	0.0007	–13834.5	0.01978	2	55309.9582	0.0002	–8069.5	0.00656	8
53179.6159	0.0009	–13829	0.01490	2	56540.3713	0.0050	–4743	–0.00163	9
53198.4841	0.0004	–13778	0.01902	2	56799.4766	0.0067	–4042.5	–0.00052	10
53203.4748	0.0005	–13764.5	0.01625	1	57132.5591	0.0020	–3142	0.00085	11
53204.5877	0.0005	–13761.5	0.01947	2	57516.5008	0.0060	–2104	0.00228	11
53208.4701	0.0006	–13751	0.01814	2	58288.8163	0.0004	–16	–0.00139	12
53223.4501	0.0003	–13710.5	0.01779	2	58288.8172	0.0002	–16	–0.00045	12
53227.5205	0.0003	–13699.5	0.01940	2	58290.8506	0.0002	–10.5	–0.00142	12
53229.3671	0.0025	–13694.5	0.01662	1	58290.8517	0.0003	–10.5	–0.00029	12
53229.5522	nr[b]	–13694	0.01678	1	58290.8525	0.0003	–10.5	0.00046	12
53230.4812	0.0004	–13691.5	0.02106	2	58292.7001	0.0002	–5.5	–0.00133	12
53242.4995	0.0006	–13659	0.01812	2	58292.7011	0.0001	–5.5	–0.00036	12
53250.4519	0.0008	–13637.5	0.01800	1	58292.7021	0.0004	–5.5	0.00069	12
53258.4049	0.0004	–13616	0.01848	2	58292.8844	0.0003	–5	–0.00196	12
53617.3741	0.0011	–12645.5	0.01462	3	58292.8854	0.0002	–5	–0.00099	12
53941.3920	0.0010	–11769.5	0.01357	4	58292.8864	0.0002	–5	–0.00002	12
54316.4573	0.0002	–10755.5	0.01580	2	58294.7343	0.0003	0	–0.00155	12
54328.4762	0.0003	–10723	0.01351	2	58294.7363	0.00027	0	0.00048	12
54331.4360	0.0002	–10715	0.01422	2	58294.7369	0.00027	0	0.00102	12
54333.4700	0.0001	–10709.5	0.01382	2	58294.9196	0.0002	0.5	–0.00118	12
54364.3497	0.0050	–10626	0.00817	5	58294.9206	0.0001	0.5	–0.00021	12
54623.6415	0.0002	–9925	0.01088	2	58294.9216	0.0003	0.5	0.00084	12
54626.5978	0.0006	–9917	0.00807	2					

[a] *ETD = Eclipse Time Difference.* [b] *Not reported. References: 1. Blättler and Diethelm (2004); 2. SuperWASP; 3. Diethelm (2006); 4. Diethelm (2007); 5. Diethelm (2008); 6. Nelson (2010); 7. Diethelm (2010); 8. Nelson (2011); 9. Hübscher (2014); 10. Hübscher and Lehmann (2015); 11. Hübscher (2017); 12. This study at DBO. This table is available through the AAVSO ftp site at ftp://ftp.aavso.org/public/datasets/Alton-eicmi-tab6.txt (if necessary, copy and paste link into the address bar of a web browser).*

Included with the ToM data summarized in Table 5 are 51 new values (BVI_cR_c) acquired at DBO, 19 times which were gathered from the literature, and five others that were extracted from period-folded LCs from the NSVS (0.298301 ± 0.000012 d) and ASAS (0.298302 ± 0.000006 d) surveys. Accordingly a new linear ephemeris (Equation 5) was calculated from near-term eclipse timings (2015–2018):

$$\text{Min.I (HJD)} = 2458464.7666\,(2) + 0.2983068\,(1)\,\text{E}. \quad (5)$$

When all data were included (1999–2018) a quadratic relationship (Equation 6) was established after plotting (Figure 7) the difference between the observed eclipse times and those predicted by the linear ephemeris against epoch such that:

$$\text{ETD} = 1.681 \pm 1.95 \cdot 10^{-4} + 6.335 \pm 1.125 \cdot 10^{-7}\,\text{E} + 1.283 \pm 0.055 \cdot 10^{-10}\,\text{E}^2. \quad (6)$$

Since the quadratic coefficient is positive ($+1.283 \cdot 10^{-10}$), in this case the ETD residuals vs. epoch suggests that the orbital period has been increasing ($0.027\,(1)\,\text{s} \cdot \text{y}^{-1}$).

3.1.4. V1309 Her

Photometric data for V1309 Her were initially obtained from the ROTSE-I survey between 1999 and 2000 (Akerlof *et al.* 2000; Woźniak *et al.* 2004; Gettel *et al.* 2006) and thereafter classified as a WUMa-type variable, according to Hoffman *et al.* (2009). Between 2005 and 2013 the Catalina Sky Survey (Drake *et al.* 2014) also included photometric data from V1309 Her. This system was also imaged during the SuperWASP (Butters *et al.* 2010) survey in 2004 and 2006–2008. As previously described for NSVS 3092802, in some cases the cadence and LC quality were sufficiently high to determine new ToM values. The light curve derived from photometric data collected at DBO included 17 new ToM measurements which are summarized in Table 6. These results along with other published eclipse timings (Table 6) were used

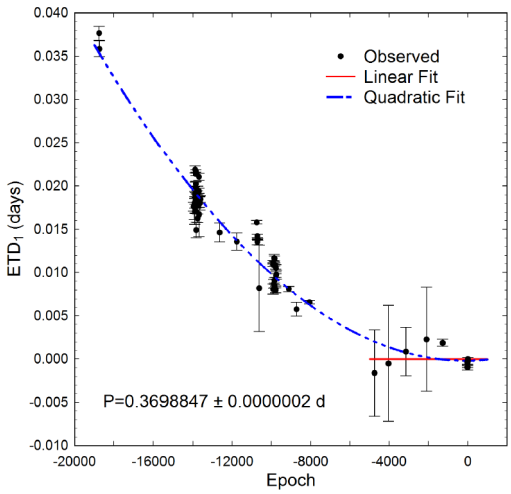

Figure 8. Eclipse timing differences (ETD) vs. epoch for V1309 Her calculated using the updated linear ephemeris (Equation 7). Measurement uncertainty is denoted by the hatched vertical lines. The solid red line within the figure indicates the linear fit while the blue dashed line represents the quadratic fit (Equation 8) from all data.

to calculate a new linear ephemeris (Equation 7) based on data acquired between 2015 and 2018:

$$\text{Min.I(HJD)} = 2458294.7356(5) + 0.3698846(2)\,E. \quad (7)$$

Secular analysis of potential period variations benefited significantly by the addition of eclipse timings captured by the SuperWASP survey (Butters *et al.* 2010). When all ToM data were included (1999–2018), plotting (Figure 8) the difference between the observed eclipse times and those predicted by the linear ephemeris against epoch reveals what appears to be a quadratic relationship (Equation 8) where:

$$\text{ETD} = -2.00 \pm 6.295 \cdot 10^{-4} + 2.211 \pm 1.511 \cdot 10^{-6}\,E + 1.023 \pm 0.090 \cdot 10^{-10}\,E^2. \quad (8)$$

In this case the ETD residuals vs. epoch can be described by an expression with a positive quadratic coefficient ($+1.023 \cdot 10^{-10}$), suggesting that the orbital period has been slowly increasing over time at the rate of $0.017(2)\,s \cdot y^{-1}$. This value, but not the sign for Q, would be refined as described below.

Another orbital period change was discovered which appears to be sinusoidal in nature and embedded within the residuals remaining after the initial quadratic fit (Equation 8). Cyclic changes of eclipse timings can result from the gravitational influence of unseen companion(s), the so-called light-time effect (LiTE). It is not unreasonable to propose that V1309 Her is a ternary system since a significant number (>50%) of contact binaries observed from the Northern Hemisphere exist as multiple systems (Pribulla and Ruciński 2006). To address this possibility LiTE analyses were performed using the simplex code for MATLAB® reported by Zasche (2009).

A quadratic relationship (Equation 9) between ETD and epoch takes the general form:

$$\text{ETD}_{\text{fitted}} = c + b \cdot E + Q \cdot E^2 + \tau. \quad (9)$$

When the orbital period change is monotonic, the last term ($\tau = 0$) can be ignored. However, in this case τ from Equation 9 is expanded as follows:

$$\tau = \frac{a_{12} \sin i}{c}\left[(1-e^2)\frac{\sin(\nu+\omega)}{1+c\cdot\cos\nu} + \sin\omega\right] \quad (10)$$

Accordingly, the associated parameters in the LITE equation (Irwin 1959) were derived, which include parameter values for P_3 (orbital period of star 3 and the 1–2 pair about their common barycenter), orbital eccentricity e, argument of periapsis ω, true anomaly ν, time of periastron passage T_0, and amplitude $A = a_{12} \sin i_3$. In this case a_{12} is the semi-major axis of the 1–2 pair's orbit about the three-star system center of mass, and i_3 is the orbital inclination of the putative third body in a three-star system.

Two viable solutions (Table 7) were produced using the Zasche *et al.* (2009) code for simplex optimization. The first (LITE-1; Figure 9) was derived with a circular orbit ($e = 0$) and the second where e was allowed to freely vary (LITE-2; Figure 10). Strictly based on the sum of squared residuals, the best fit was with an elliptical orbit (LITE-2) although the other parameter estimates where $e = 0$ may not be meaningfully different. The LITE-2 results are consistent with a putative third body orbiting elliptically ($e = 0.83 \pm 0.18$) every ~9.5 y at a distance no farther than 4.9 ± 1.1 A.U. from the common center of gravity. The minimum mass of a coplanar ($i_3 = 90°$) orbiting third body was calculated to be $\sim 0.126 \pm 0.001\,M_\odot$ based on the derived mass function ($f(M_3) = 0.0072 \pm 0.0001$). The corresponding added luminosity (L_3) of a third main sequence star was estimated to be ~0.03% according to Equation 11, where M_{min} is the estimated minimum mass ($i_3 = 90°$):

$$L_3(\%) = \frac{100 \cdot M_{min}^{3.5}}{L_1 + L_2 + M_{min}^{3.5}}. \quad (11)$$

This very small percent contribution of light would not be expected nor did it require adjustment by the WD2003 code third light parameter ($l_3 = 0$) in order to accurately simulate the LC model fits around minimum light (section 3.4).

Modulated changes in the orbital period can also result from magnetic activity cycles or apsidal motion of a binary pair. Since contact binary systems are tidally locked with circular orbits, apsidal motion can be immediately eliminated from consideration. Short-period binaries are magnetically very active due to the formation of photospheric starspots, chromospheric plages, and other high energy disturbances (Berdyugina 2005). The corresponding hydromagnetic dynamo can produce changes in the gravitational quadrupole moment of the active star via redistribution of the internal angular momentum with corresponding changes in the magnetic torque within the stellar convective zone. When the gravitational quadrupole moment of the active component increases, its companion experiences a stronger gravitational force which then moves closer to the system barycenter. The orbital period will decrease according to this scenario. By contrast, when the

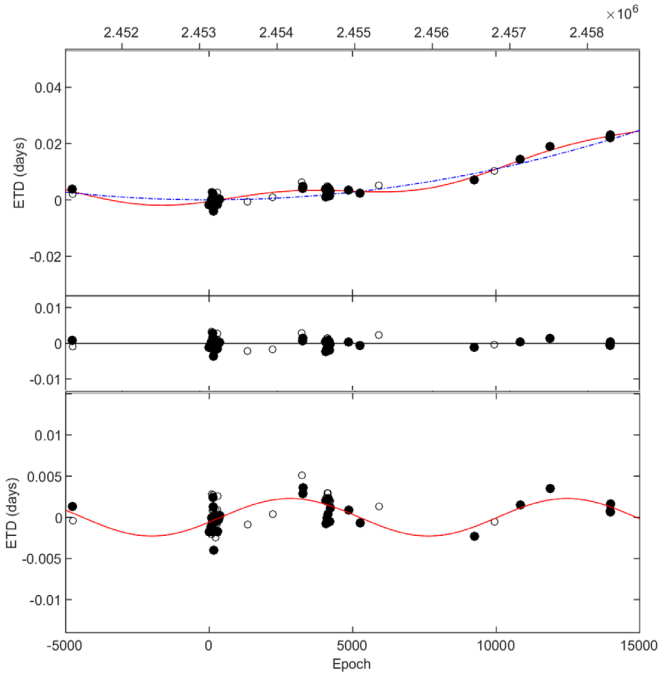

Figure 9. LITE-1 fit (Table 7) using eclipse timing differences (ETD) determined for V1309 Her between 1999 and 2018. The solid red line in the top panel describes the fit for circular (e=0) orbit (P_3=9.78 y) of a putative third body while the dashed blue line defines the quadratic fit from the eclipse timing residuals. Solid circles (●) represent times at Min I whereas open circles (○) indicate times at Min II. The middle panel illustrates the total residuals remaining after LITE analysis, and the bottom panel depicts the modeled fit after subtracting out the quadratic component.

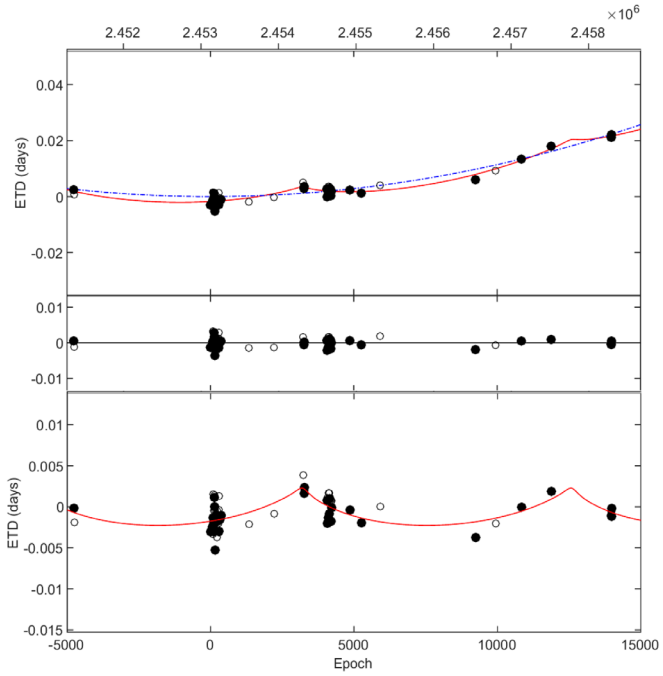

Figure 10. LITE-2 fit (Table 7) using eclipse timing differences (ETD) determined for V1309 Her between 1999 and 2018. The solid red line in the top panel describes the fit for an elliptical (e = 0.83) orbit (P_3=9.5 y) of a putative third body while the dashed blue line defines the quadratic fit from the eclipse timing residuals. Solid circles (●) represent times at Min I whereas open circles (○) indicate times at Min II. The middle panel illustrates the total residuals remaining after LiTE analysis, and the bottom panel depicts the modeled fit after subtracting out the quadratic component.

gravitational quadrupole moment of the active star weakens, the orbital period increases. A detailed examination of the energetics ($\Delta E/E_{sec}$) required to produce this effect attributed to Applegate (1992) was performed according to Völschow *et al.* (2016) and the accompanying "Eclipse Time Variation Calculator" webmodule (http://theory-starformation-group.cl/applegate/index.php). $\Delta E/E_{sec}$ is defined as the energy required to drive the Applegate mechanism divided by the available energy produced in the magnetically active star. This value determines whether the Applegate mechanism is energetically feasible. Solutions are provided from the two-zone model and the constant density model by Völschow *et al.* (2016), along with a solution based on the thin-shell model by Tian *et al.* (2009). Tian *et al.* (2009) derived a relationship between the energetics necessary to drive the Applegate mechanism and the observed variability in eclipse timings:

$$\frac{\Delta E}{E_{sec}} = 0.233 \cdot \left(\frac{M_{sec}}{M_\odot}\right)^{3} \cdot \left(\frac{R_{sec}}{R_\odot}\right)^{-10} \cdot \left(\frac{T_{sec}}{6000\ K}\right)^{-4} \cdot \left(\frac{a_{bin}}{R_\odot}\right)^{4} \cdot \left(\frac{\Delta P}{s}\right)^{2} \cdot \left(\frac{P_{mod}}{y}\right)^{-1}. \quad (12)$$

The measureables in this case include the secondary mass (M_{sec}), radius (R_{sec}), temperature (T_{sec}), semi-major axis of the binary pair (a_{bin}), the modulation period of the binary pair (P_{mod}), and ΔP where:

$$\frac{\Delta P}{P_{bin}} = 2\pi \left(\frac{O-C}{P_{mod}}\right). \quad (13)$$

Since the $\Delta E/E_{sec}$ value (0.0228) was below one, then this would energetically favor orbital period modulations that arise from the Applegate mechanism.

The two-zone model provides two solutions, one requiring more energy and one requiring less energy. Therein the finite shell two-zone model accounts for all essential physics involved with the Applegate effect from main-sequence low mass companions (0.1–0.6 $M_\odot$). Accordingly the latter energy solution is:

$$\frac{\Delta E^{-}}{E_{sec}} = k_1 \cdot \frac{M_{sec} R_{sec}^2}{P_{bin}^2 P_{mod} L_{sec}} \cdot \left(1 \pm \sqrt{(1 - k_2 G) \frac{a_{bin}^2 M_{sec} P_{bin}^2}{R_{sec}^5}} \frac{\Delta P}{P_{bin}}\right)^2, \quad (14)$$

wherein k_1 is assigned a value of 0.133 and k_2 is 3.42. Since the calculated value for $\Delta E^{-} / E_{sec}$ is less than unity (0.422), this model also indicates that V1309 Her is a potential candidate for orbital period modulation by magnetic cycles.

The apparent sinusoidal-like behavior is supported by data collected over the past 19 years, which is only equal to two cycles of orbital period variation. Therefore, some caution should be exercised such that these findings are considered preliminary and not a definitive solution. Moreover, at this time

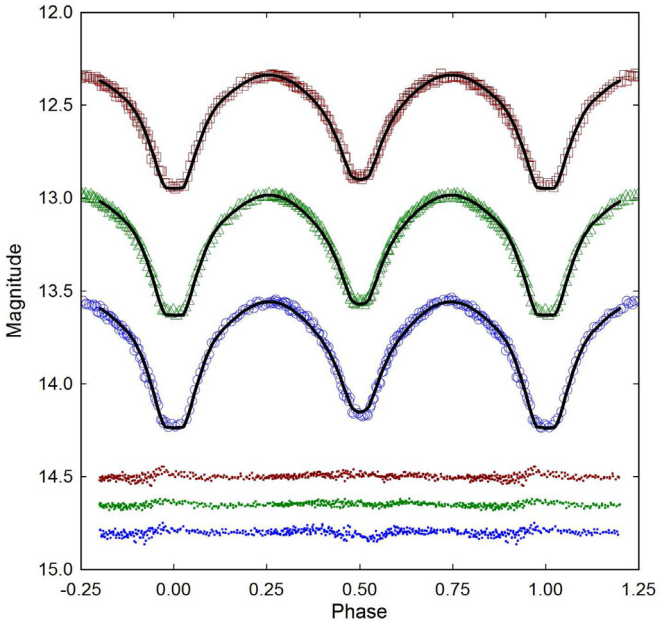

Figure 11. Period-folded (0.3625350 ± 0.0000001 d) CCD light curves for EI CMi produced from photometric data collected at DBO between December 21, 2018, and February 7, 2019. The top (I_c), middle (V) and bottom curve (B) shown above were reduced to MPOSC3-based catalog magnitudes using MPO CANOPUS. In this case, the Roche model assumed an W-subtype overcontact binary with no spots; residuals from the model fits are offset at the bottom of the plot to keep the values on scale.

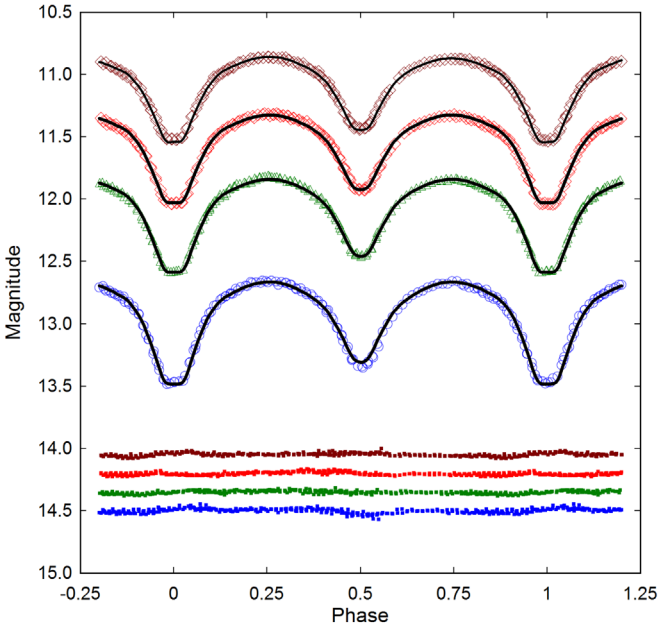

Figure 13. Period-folded (0.2983068 ± 0.0000001 d) CCD light curves for V958 Mon produced from photometric data obtained at DBO between November 27, 2018, and December 12, 2018. Starting from top to bottom the I_c, R_c, V, and B light curves were reduced to APASS DR9 catalog magnitudes using MPO CANOPUS. In this case, the Roche model assumed a W-type overcontact binary; residuals from the model fits are offset at the bottom of the plot to keep the values on scale.

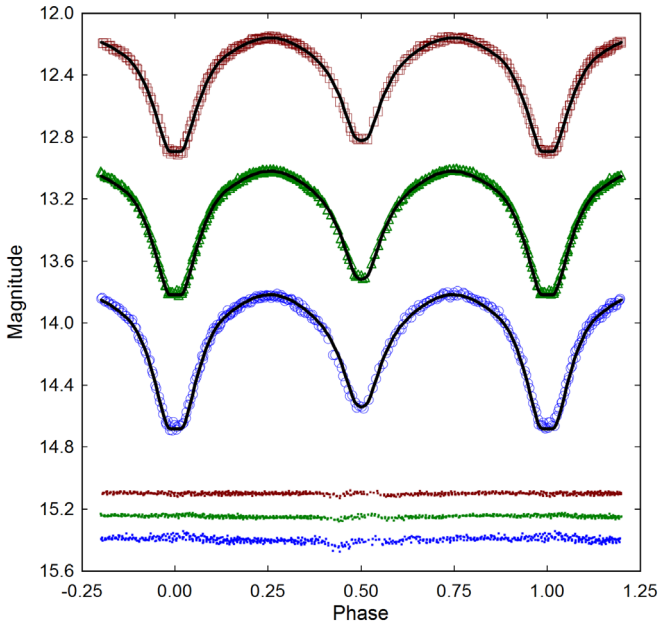

Figure 12. Period-folded (0.3161697 ± 0.0000001 d) CCD light curves acquired from NSVS 3092802 at DBO between September 22, 2018, and June 03, 2019. The top (I_c), middle (V) and bottom curve (B) shown above were reduced to MPOSC3-based catalog magnitudes using MPO CANOPUS. In this case, the Roche model assumed an W-subtype overcontact binary with no spots; residuals from the model fits are offset at the bottom of the plot to keep the values on scale.

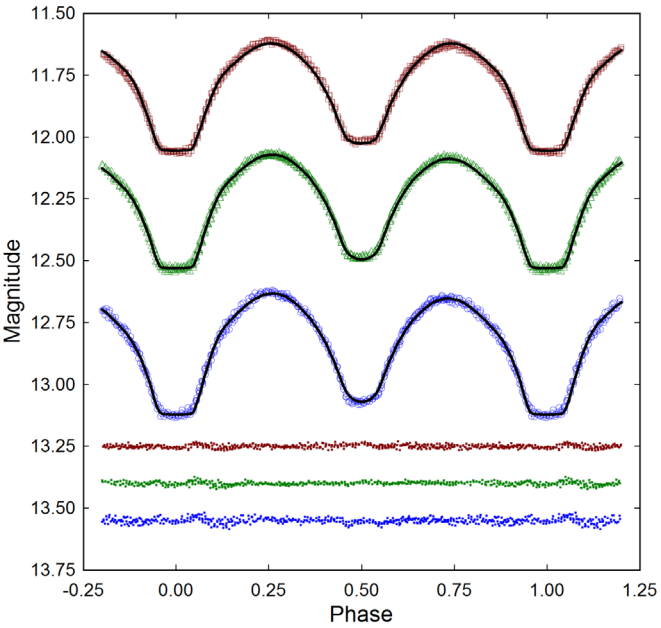

Figure 14. Period-folded (0.3698847 ± 0.0000002 d) CCD light curves for V1309 Her obtained at DBO between June 21, 2018, and June 25, 2018. The top (I_c), middle (V), and bottom curves (B) were reduced to APASS DR9 catalog magnitudes using MPO CANOPUS. The Roche model assumed a W-type overcontact binary with one cool spot on each star; residuals from the model fits are offset at the bottom of the plot to keep the values on scale.

Table 7. Orbital period modulation (P_3) and putative third-body solution to the light-time effect (LiTE) observed from changes in V1309 Her eclipse timings.

Parameter	*Units*	*LiTE-1*[a]	*LiTE-2*[b]
HJD0–2400000		53121.5485 ± 0.0003	53121.5498 ± 0.0003
P_3	(y)	9.78 ± 0.37	9.50 ± 0.39
ω		0.000651 ± 0.000025	0.000670 ± 0.000027
A (semi-ampl.)	(d)	0.0023 ± 0.0008	0.0023 ± 0.0005
ω	(°)	—	103.6 ± 22.3
e_3		0 ± 0.136	0.83 ± 0.18
a'_{12} sin i'	(a.u.)	0.3949 ± 0.1374	0.4013 ± 0.0859
$f(M_3)$(mass func.)	($M_\odot$)	0.00064 ± 0.00012	0.00072 ± 0.00001
M_3 (i=90°)	($M_\odot$)	0.121 ± 0.008	0.126 ± 0.001
M_3 (i=60°)	($M_\odot$)	0.141 ± 0.008	0.146 ± 0.001
M_3 (i=30°)	($M_\odot$)	0.255 ± 0.016	0.265 ± 0.001
Q (quad. coeff.)	(10^{-10})	1.0964 ± 0.0001	1.141 ± 0.0001
Sum of squared residuals		0.00134781	0.00120855

[a] *Zasche* et al. *(2009)—simplex optimization with third body circular orbit.* [b] *Zasche* et al. *(2009)—simplex optimization with third body elliptical orbit.*

it is not possible to firmly establish whether the gravitational effect of a third body or variations in the quadrupole moment is responsible for cyclic changes in the orbital period of V1309 Her. Unfortunately, without other supporting evidence such as might be derived from space-based spectro-interferometry and/or direct imaging, secular analyses still leaves us with two equally plausible but distinctly different phenomenological origins for cyclic modulation of the dominant orbital period.

3.2. Effective temperature estimation

The effective temperature (T_{eff1}) of the more massive, and therefore most luminous component (defined as the primary star herein) was derived from a composite of astrometric (USNO-A2.0, USNO-B1.0, and UCAC4) and photometric (2MASS, SDSS-DR8, and APASS) survey measurements that were as necessary transformed to (B–V) (http://www.aerith.net/astro/color_conversion.html; http://brucegary.net/dummies/method0.html). Interstellar extinction (A_V) and reddening ($E(B–V) = A_V / 3.1$) were estimated for targets within the Milky Way Galaxy according to the procedure described by Amôres and Lepine (2005). This model, which is simulated in a Linux-based companion program (ALEXTIN; http://www.galextin.org/explain.html), requires the Galactic coordinates (*l, b*) and the distance in kpc (Bailer-Jones 2015). After subtracting out reddening to arrive at a value for intrinsic color, $(B–V)_0$, T_{eff1} estimates were interpolated for each system using the values reported for main sequence dwarf stars by Pecaut and Mamajek (2013). Additional sources used to establish a median value for each T_{eff1} included low resolution spectra obtained from LAMOST-DR5 (Zhao *et al.* 2012; Rui *et al.* 2019), the Gaia DR2 release of stellar parameters (Andrae *et al.* 2018), and an empirical relationship (Houdashelt *et al.* 2000) based on intrinsic color where $0.32 \leq (B–V)_0 \leq 1.35$. The median results, summarized in Table 8, were adopted for Roche modeling of LCs from each binary system.

3.3. Roche modeling approach

Roche modeling of LC data from all four OCBs was initially performed with PHOEBE 0.31a (Prša and Zwitter 2005) and then refined using WDWINT56A (Nelson 2009). Both programs feature a MS Windows-compatible GUI interface to the Wilson-Devinney WD2003 code (Wilson and Devinney 1971; Wilson 1979, 1990). WDWINT56A incorporates Kurucz's atmosphere models (Kurucz 2002) that are integrated over BVR_cI_c passbands. In all cases, the selected model was Mode 3 for an overcontact binary. Other modes (detached and semi-detached) were attempted but never approached the model fit (χ^2 value reported for each bandpass in PHOEBE 0.31a) achieved with Mode 3. With each of these variable systems, the internal energy transfer to the surface is driven by convective (7500 K) rather than radiative processes; therefore, the value for bolometric albedo ($A_{1,2} = 0.5$) was assigned according to Ruciński (1969) while the gravity darkening coefficient ($g_{1,2} = 0.32$) was adopted from Lucy (1967). Logarithmic limb darkening coefficients (x_1, x_2, y_1, y_2) were interpolated (van Hamme 1993) following any change in the effective temperature (T_{eff2}) of the secondary star during model fit optimization using differential corrections (DC). All but the temperature of the more massive star (T_{eff1}), $A_{1,2}$ and $g_{1,2}$ were allowed to vary during DC iterations. In general, the best fits for T_{eff2}, i, q, and Roche potentials ($\omega_1 = \omega_2$) were collectively refined (method of multiple subsets) by DC using the multicolor LC data until a simultaneous solution was found. Not uncommon for OCB systems, LCs from V1309 Her exhibit varying degrees of asymmetry during quadrature (Max I > Max II) which is often called the O'Connell effect (O'Connell 1951). Surface inhomogeneity often attributed to star spots was addressed in V1309 Her by the addition of two cool spots to obtain the best fit LC simulations. Only EI CMi required third light correction ($l_3 > 0$) to improve Roche model fits. Since each system clearly undergoes a total eclipse, Roche model convergence to a unique value for q is expected according to Terrell and Wilson (2005), thereby obviating the need for any formal "q-search" exercise. These general findings are described in more detail within the subsections for each variable that follow.

3.4. Roche modeling results

Without radial velocity (RV) data it is generally not possible to unambiguously determine the mass ratio, subtype (A or W), or total mass of an eclipsing binary system. Nonetheless since

Table 8. Estimation of effective temperature (T_{eff1}) of the primary star in EI CMi, NSVS 3092802, V958 Mon, and V1309 Her.

	EI CMi	*NSVS 3092802*	*V958 Mon*	*V1309 Her*
DBO $(B–V)_0$	0.461 ± 0.019	0.741 ± 0.015	0.797 ± 0.025	0.532 ± 0.013
Median combined $(B–V)_0$[a]	0.534 ± 0.052	0.759 ± 0.036	0.846 ± 0.020	0.505 ± 0.004
Galactic reddening (E(B–V))	0.110 ± 0.007	0.054 ± 0.001	0.031 ± 0.001	0.031 ±0.002
Survey T_{eff1}[b] (K)	6130 ± 209	5410 ± 100	5250 ± 65	6160 ± 11
Gaia T_{eff1}[c] (K)	5757^{+441}_{-195}	5789^{+380}_{-68}	5005^{+133}_{-98}	6592^{+609}_{-525}
Houdasheldt T_{eff1}[d] (K)	6102 ± 276	5405 ± 308	5174 ± 330	6121 ± 212
LAMOST DR5 T_{eff1}[e] (K)	5866 ± 215	—	5201 ± 20	6233 ± 19
Median T_{eff1} (K)	5980 ± 246	5410 ± 224	5190 ± 90	6196 ± 115
Spectral Class	F6V[f]	G8V-G9V[g]	G8V[f]	F4V[f]

[a] Surveys and DBO intrinsic $(B–V)_0$ determined using reddening values (E(B–V)) from each star. [b] T_{eff1} interpolated from median combined $(B–V)_0$ using Table 4 in Pecaut and Mamajek (2013). [c] Values from Gaia DR2 (http://vizier.u-strasbg.fr/viz-bin/VizieR?-source=I/345/gaia2). [d] Values calculated with Houdasheldt (2000) empirical relationship. [e] Values from LAMOST DR5 (http://dr5.lamost.org/search). [f] Spectral class from LAMOST DR5. [g] Spectral class interpolated from median combined $(B–V)_0$: Pecaut and Mamajeck (2013).

a total eclipse is observed in the LCs from all four systems, a unique mass ratio value for each system could be found (Terrell and Wilson 2005). Standard errors reported in Tables 9–12 are computed from the DC covariance matrix and only reflect the model fit to the observations which assume exact values for any fixed parameter. These errors are generally regarded as unrealistically small, considering the estimated uncertainties associated with the mean adopted T_{eff1} values along with basic assumptions about $A_{1,2}$, $g_{1,2}$ and the influence of spots added to the Roche model. Normally, the value for T_{eff1} is fixed with no error during modeling with the WD code despite measurement uncertainty which can arguably approach 10% relative standard deviation (R.S.D.) without supporting spectral data. The effect that such uncertainty in T_{eff1} would have on modeling estimates for q, i, $\omega_{1,2}$, and T_{eff2} has been investigated with other overcontact binaries including A- (Alton 2019; Alton *et al.* 2020) and W-subtypes (Alton and Nelson 2018). As might be expected any change in the fixed value for T_{eff1} results in a corresponding change in the T_{eff2}. These findings are consistent whereby the uncertainty in the model fit for T_{eff2} would be essentially the same as that established for T_{eff1}. Furthermore, varying T_{eff1} by as much as 10% did not appreciably affect the uncertainty estimates (R.S.D. < 2.2%) for i, q or $\omega_{1,2}$ (Alton 2019; Alton and Nelson 2018; Alton *et al.* 2020). Assuming that the actual T_{eff1} values for each of the four OCBs investigated herein fall within 10% of the adopted values used for Roche modeling (a reasonable expectation based on T_{eff1} data provided in Table 8), then uncertainty estimates for i, q or $\omega_{1,2}$ along with spot size, temperature, and location would likely not exceed 2.2% R.S.D.

The fill-out parameter (f) which corresponds to the outer surface shared by each star was calculated according to Equation 15 (Kallrath and Milone 1999; Bradstreet 2005) where:

$$f = (\omega_{inner} - \omega_{1,2}) / (\omega_{inner} - \omega_{outer}) , \quad (15)$$

wherein ω_{outer} is the outer critical Roche equipotential, ω_{inner} is the value for the inner critical Roche equipotential, and $\omega = \omega_{1,2}$ denotes the common envelope surface potential for the binary system. In all cases the systems are considered overcontact since $0 < f < 1$.

3.4.1. EI CMi

LC parameters, geometric elements, and their corresponding uncertainties are summarized in Table 9. According to Binnendijk (1970) the deepest minimum (Min I) of a W-type overcontact system occurs when a cooler more massive constituent occludes its hotter but less massive binary partner. The flattened-bottom dip in brightness that is sustained for 0.43 h at Min I (Figure 11) indicates a total eclipse of the secondary star; WD modeling proceeded under the assumption that EI CMi is a W-subtype. Since according to the convention used herein whereby the primary star is the most massive ($m_2 / m_1 \leq 1$), a phase shift (0.5) was introduced to properly align the LC for subsequent Roche modeling. These assumptions proved to be similarly true for NSVS 3092802, V958 Mon, and V1309 Her and will not be repeated in their respective subsections. It should also be noted that larger model fit residuals around minimum light are observed where photometric values are expected to be most variable.

It quickly became obvious that model-simulated LCs at Min I and Min II were consistently deeper than the observed values in all three bandpasses. This was rectified by allowing the third light parameter (l_3) to freely vary during DC optimization. These findings (Table 9) suggest the presence of a blue-rich ($l_3(B) > l_3(V) > l_3(I_c)$) field star in the distant background that has contaminated light arriving from EI CMi. Potential secular changes in the orbital period that might arise from the influence of a third gravitational body cannot be evaluated at this time due to the limited availability of precise eclipse timing data. Despite the lack of supporting evidence for a stellar body in close proximity, the presence of a hot main sequence star in the same neighborhood as EI CMi would likely overwhelm any photometric measurement, thereby discounting this possibility. Nonetheless, it is still possible that a nearby faint blue object such as a cool (T_{eff} < 8000 K) white dwarf could satisfactorily explain the blue-rich third light.

A three-dimensional rendering (Figure 15) using BINARY MAKER 3 (BM3; Bradstreet and Steelman 2004) with the final WDWINT56A modeling results illustrates the secondary star transit across the primary face during Min II ($\Phi = 0.5$), thereby confirming that the secondary star is totally eclipsed at Min I.

Table 9. Lightcurve parameters evaluated by Roche modeling and the geometric elements derived for EI CMi assuming it is a W-subtype W UMa-type eclipsing variable with no spots.

Parameter[a]	*Observed*
T_{eff1} (K)[b]	5980
T_{eff2} (K)	6314 (4)
q (m_2 /m_1)	0.436 (1)
A[b]	0.50
g[b]	0.32
$\omega_1 = \omega_2$	2.671 (4)
i°	89 (1)
$L_1 / (L_1 + L_2)B$[c]	0.6034 (4)
$L_1 / (L_1 + L_2)V$	0.6226 (2)
$L_1 / (L_1 + L_2)I_c$	0.6388 (2)
l_3 (B)[d]	1.166 (5)
l_3 (V)	0.890 (4)
l_3 (c)	0.733 (4)
r_1 (pole)	0.4401 (5)
r_1 (side)	0.4724 (6)
r_1 (back)	0.5056 (7)
r_2 (pole)	0.3043 (12)
r_2 (side)	0.3198 (15)
r_2 (back)	0.3643 (29)
Fill-out factor (%)	30.0
RMS (B)[e]	0.01280
RMS (V)	0.00834
RMS (I_c)	0.00978

[a] All uncertainty estimates for T_{eff2}, q, $\omega_{1,2}$, i, $r_{1,2}$, and L_1 from WDWINT56A (Nelson 2009). [b] Fixed with no error during DC. [c] L_1 and L_2 refer to scaled luminosities of the primary and secondary stars, respectively. [d] fractional percent luminosity of third light parameter (l_3) at $\Phi = 0.25$. [e] Monochromatic residual mean square error from observed values.

Table 10. Lightcurve parameters evaluated by Roche modeling and the geometric elements derived for NSVS 3092802 assuming it is a W-subtype W UMa-type eclipsing variable with no spots.

Parameter[a]	*Observed*
T_{eff1} (K)[b]	5410
T_{eff2} (K)	5693 (2.2)
q (m_2 / m_1)	0.521 (1)
A[b]	0.50
g[b]	0.32
$\omega_1 = \omega_2$	2.88 (2)
i°	88.4 (3)
$L_1 / (L_1 + L_2)B$[c]	0.5678 (3)
$L_1 / (L_1 + L_2)V$	0.5875 (1)
$L_1 / (L_1 + L_2)I_c$	0.6034 (1)
r_1 (pole)	0.4163 (2)
r_1 (side)	0.4430 (3)
r_1 (back)	0.4734 (4)
r_2 (pole)	0.3087 (6)
r_2 (side)	0.3232 (8)
r_2 (back)	0.3593 (13)
Fill-out factor (%)	10.7
RMS (B)[d]	0.00849
RMS (V)	0.00479
RMS (I_c)	0.00412

[a] All uncertainty estimates for T_{eff2}, q, $\omega_{1,2}$, i, $r_{1,2}$, and L_1 from WDWINT56A (Nelson 2009). [b] Fixed with no error during DC. [c] L_1 and L_2 refer to scaled luminosities of the primary and secondary stars, respectively. [d] Monochromatic residual mean square error from observed values.

Table 11. Lightcurve parameters evaluated by Roche modeling and the geometric elements derived for V958 Mon assuming it is a W-type W UMa variable.

Parameter[a]	*DBO No spot*	*Michaels*[b] *2016*
T_{eff1} (K)[c]	5150	5465 (3)
T_{eff2} (K)	5510 (3)	5111
q (m_2 / m_1)	0.434 (1)	2.25 (2)
A[c]	0.50	0.5
g[c]	0.32	0.32
$\omega_1 = \omega_2$	2.734 (2)	5.489 (26)
i°	85.2 (3)	86.4 (4)
$A_P = T_S / T_{star}$[d]	—	1.17 (4)
θ_P (spot co-latitude)[d]	—	113 (2)
Φ_P (spot longitude)[d]	—	356 (1)
r_p (angular radius)[d]	—	12 (2)
$L_1 / (L_1 + L_2)B$[e]	0.5854 (5)	—
$L_1 / (L_1 + L_2)V$	0.6092 (2)	0.4101 (4)
$L_1 / (L_1 + L_2)R_c$	0.6222 (5)	—
$L_1 / (L_1 + L_2)I_c$	0.6308 (3)	—
l_3(V)	—	0.0121 (42)
r_1 (pole)	0.4283 (3)	—
r_1 (side)	0.4568 (4)	0.3103 (7)
r_1 (back)	0.4849 (5)	—
r_2 (pole)	0.2913 (3)	—
r_2 (side)	0.3042 (3)	0.4884 (39)
r_2 (back)	0.3384 (5)	—
Fill-out factor (%)	5.1	19
RMS (B)[f]	0.01048	—
RMS (V)	0.00826	—
RMS (R_c)	0.01024	—
RMS (I_c)	0.00803	—

[a] All DBO uncertainty estimates for T_{eff2}, q, $\omega_{1,2}$, i, $r_{1,2}$, and L_1 from WDWINT56A (Nelson 2009). [b] Spotted solution only presented; primary defined as hotter, not more massive star (q > 1). [c] Fixed with no error during DC. [d] Secondary star spot parameters in degrees (θ_p, Φ_p, and r_p) or A_p in fractional degrees (K). [e] L_1 and L_2 refer to scaled luminosities of the primary and secondary stars, respectively. [f] Monochromatic residual mean square error from observed values.

3.4.2. NSVS 3092802

LC parameters and geometric elements with their associated uncertainty for this W-subtype W UMa-type binary can be found in Table 10. During this epoch, model fits at minimum and maximum (Max I ~ Max II) light did not require the addition of spots. As expected for a system exhibiting a total eclipse at Min I, a three-dimensional rendering produced using BM3 (Figure 16) shows a transit of the hotter secondary across the face of the primary star during Min II ($\Phi = 0.5$).

3.4.3. V958 Mon

Unlike the other three OCB systems reported herein, multi-color (V, g', r', and i') LCs for V958 Mon have been published (Michaels 2016). It should be noted therein, the primary star is defined as the hotter binary partner and not the more massive entity. The corresponding LC parameters and geometric elements derived from Roche modeling with the WD code are summarized in Table 11 along with new results from this investigation. Michaels (2016) adopted a slightly lower T_{eff} for the more luminous star, however, this was not expected to produce any meaningful difference (Alton *et al.* 2020) where comparisons could be made. In general these findings compare favorably with regard to mass ratio (1 / q = 0.444 vs. 0.434) and orbital inclination (86.4 vs. 85.3°). Model fits for the LC data

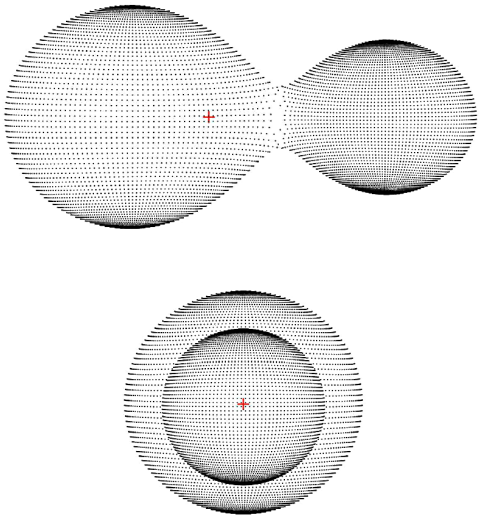

Figure 15. Three-dimensional spatial model of EI CMi illustrating (top) the mutually shared (f = 0.3) atmosphere of the binary system and (bottom) the secondary star transit across the primary star face at Min II (Φ = 0.5).

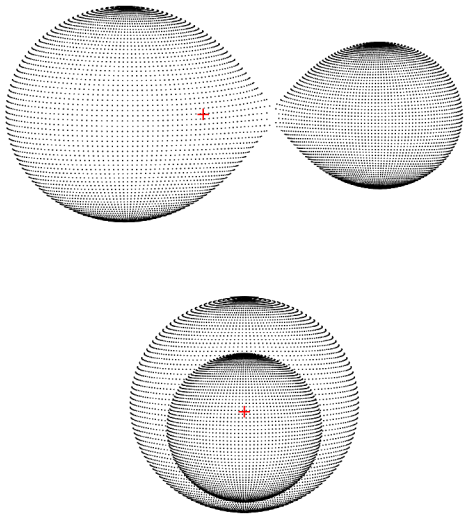

Figure 17. Three-dimensional spatial model of V958 Mon during 2018–2019 illustrating (top) the shallow contact (f = 0.05) between both stars and the secondary star transit across the primary star face at Min II (Φ = 0.5).

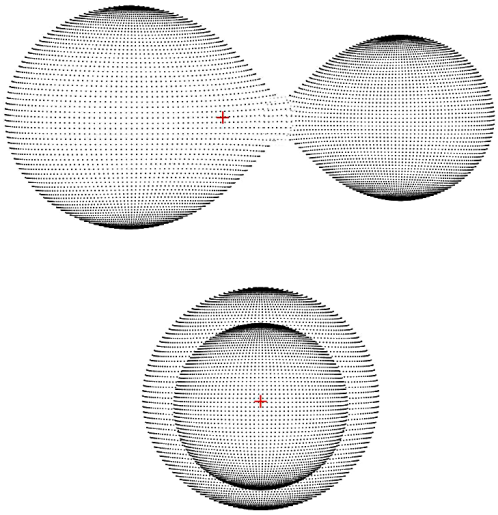

Figure 16. Three-dimensional spatial model of NSVS 3092802 illustrating (top) the mutually shared (f = 0.107) atmosphere of the binary system and (bottom) the secondary star transit across the primary star face at Min II (Φ = 0.5).

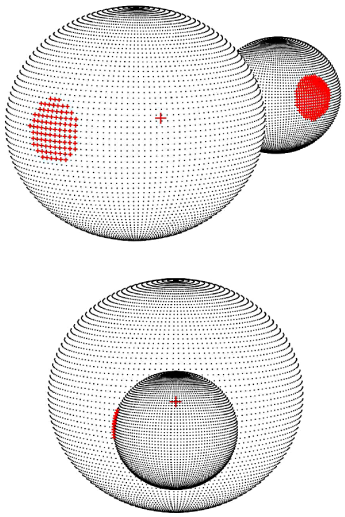

Figure 18. Three-dimensional spatial model of V1309 Her during 2018 illustrating (top) the location of each cool spot and (bottom) the secondary star transit across the primary star face at Min II (Φ = 0.5).

acquired at DBO did not show any meaningfully significant improvement by the addition of a spot. LCs produced by Michaels (2016) were best fit by the addition of a hot spot on the more massive star, a difference that is not uncommon given these photometric data were collected three years earlier. A three-dimensional rendering of the DBO modeled data produced using BM3 (Figure 17) shows a transit of the hotter secondary across the primary star face during Min II (Φ = 0.5), an observation consistent with a total eclipse at Min I. The most significant difference is that Michaels (2016) invoked third light (l_3) presumably to improve the simulated fits at Min I and Min II, whereas the DBO-derived data did not require this additional parameter ($l_3 = 0$). There are an insufficient number of eclipse timings to propose the presence of a dim third body (section 3.1.3.). Nonetheless, it is not obvious why LCs from the same target collected during another epoch would exhibit this behavior. In addition, the fill-out factors varied widely (~4% vs. 19%), most likely due to differences in spot location and/or adding third light ($l_3 \neq 0$) to the Roche model.

3.4.4. V1309 Her

LC parameters and geometric elements with their associated uncertainty derived from Roche modeling of this W-subtype W UMa-type binary are summarized in Table 12. During 2018, LCs exhibited significant asymmetry such that model simulations during quadrature (phase = 0.75) and at Min I were poorly fit. It is not unreasonable to assume that OCBs as a class are magnetically active and can harbor starspots. V1309 Her has been poorly studied so it is no surprise that there are no Doppler Imaging data to support the presence of spots. This can be said for the vast majority of published papers which include star spots to improve the light curve fit during Roche modeling. X-ray luminosity is commonly used as an indicator of stellar magnetic activity (Wright *et al.* 2011) and has been investigated

Table 12. Lightcurve parameters evaluated by Roche modeling and the geometric elements derived for V1309 Her assuming it is a W-type W UMa variable.

Parameter[a]	*No spot*	*Cool spot*
T_{eff1} (K)[b]	6196	6196
T_{eff2} (K)	6586 (4)	6330 (2)
q (m_2 / m_1)	0.182 (1)	0.213 (1)
A[b]	0.50	0.5
g[b]	0.32	0.3
$\omega_1 = \omega_2$	2.141 (1)	2.232 (2)
i°	86.2 (3)	82.3 (2)
$A_P = T_S / T_{star}$[c]	—	0.83 (1)
θ_P (spot co-latitude)[c]	—	87 (1)
Φ_P (spot longitude)[c]	—	177 (1)
r_P (angular radius)[c]	—	14.0 (1)
$A_S = T_S / T_{star}$[d]	—	0.87 (1)
Φ_S (spot co-latitude)[d]	—	86 (3)
Φ_S (spot longitude)[d]	—	75.5 (2.1)
r_S (angular radius)[d]	—	21.30 (24)
$L_1 / (L_1 + L_2)B$[e]	0.7591 (3)	0.7780 (2)
$L_1 / (L_1 + L_2)V$	0.7745 (1)	0.7835 (1)
$L_1 / (L_1 + L_2)I_c$	0.7884 (1)	0.7884 (1)
r_1 (pole)	0.5052 (2)	0.4899 (3)
r_1 (side)	0.5555 (4)	0.5343 (5)
r_1 (back)	0.5808 (4)	0.5596 (5)
r_2 (pole)	0.2390 (3)	0.2452 (9)
r_2 (side)	0.2504 (3)	0.2562 (11)
r_2 (back)	0.2964 (7)	0.2963 (22)
Fill-out factor (%)	39.3	23.4
RMS (B)[f]	0.01219	0.00808
RMS (V)	0.00862	0.00518
RMS (I_c)	0.01075	0.00732

[a] All uncertainty estimates for T_{eff2}, q, $\omega_{1,2}$, i, $r_{1,2}$, and L_1 from WDWINT56A (Nelson 2009). [b] Fixed with no error during DC. [c] Primary star spot parameters in degrees (θ_P, Φ_P, and r_P) or A_P in fractional degrees (K). [d] Secondary star spot parameters in degrees (θ_S, Φ_S, and r_S) or A_S in fractional degrees (K). [e] L_1 and L_2 refer to scaled luminosities of the primary and secondary stars, respectively. [f] Monochromatic residual mean square error from observed values.

in eclipsing contact binary stars (Szczygiel *et al.* 2008; Stępień *et al.* 2001). Unlike the other three systems described herein, two of which are much closer, there is circumstantial evidence that V1309 Her is magnetically active based on data acquired from the ROSAT all-sky survey (Voges *et al.* 1999). In this case an X-ray source (hardness ratio = 0.13) was detected within 2 arcsec of its optical counterpart. Aside from arriving at a mathematically convenient solution, there is physical justification for the presence of starspot(s) in order to address the light curve asymmetry exhibited by V1309 Her. In this case, a single cool spot was positioned on the primary star to deepen Min I while another cool spot was placed on the secondary star to improve the LC simulation around phase = 0.75 (Figure 18). In addition, this spatial rendering produced using BM3 shows the hotter secondary transiting across the primary star face during Min II ($\Phi = 0.5$), reaffirming that a total eclipse occurred during Min I.

According to LITE analysis (section 3.1.4), a putative third body would be too dim to detect by CCD photometry. As expected, there was no need to invoke a third light correction ($l_3 = 0$) to achieve an acceptable model fit at minimum light.

3.5. Stellar parameters

Fundamental stellar parameters were estimated for each binary system using results from the best fit LC simulations. Previous experience (Alton 2019; Alton *et al.* 2020; Alton and Nelson 2018) with other OCBs would suggest that uncertainty (R.S.D.) for each of these estimates is at least 2.2%. However, without the benefit of RV data which define the orbital motion, mass ratio, and total mass of the binary pair, these results should be considered "relative" rather than "absolute" parameters and regarded as preliminary.

Starting with EI CMi, a calculation template is described below for estimating the solar mass and size, semi-major

Table 13. Fundamental stellar parameters for EI CMi using the photometric mass ratio ($q_{ptm} = m_2 / m_1$) from Roche model fits of LC data (2018–2019) and the estimated mass based on empirically derived M-PRs for overcontact binary systems.

Parameter	*Primary*	*Secondary*
Mass ($M_\odot$)	1.17 ± 0.05	0.51 ± 0.02
Radius ($R_\odot$)	1.15 ± 0.01	0.79 ± 0.01
a ($R_\odot$)	2.54 ± 0.03	2.54 ± 0.03
Luminosity ($L_\odot$)	1.52 ± 0.25	0.89 ± 0.02
M_{bol}	4.30 ± 0.18	4.88 ± 0.02
Log (g)	4.38 ± 0.02	4.35 ± 0.02

Table 14. Fundamental stellar parameters for NSVS~3092802 using the mean photometric mass ratio ($q_{ptm} = m_2 / m_1$) from the Roche model fits of LC data (2018–2019) and the estimated mass based on empirically derived M-PRs for W UMa type variable stars}

Parameter	*Primary*	*Secondary*
Mass ($M_\odot$)	1.06 ± 0.04	0.55 ± 0.02
Radius ($R_\odot$)	1.00 ± 0.01	0.74 ± 0.01
a ($R_\odot$)	2.29 ± 0.02	2.29 ± 0.02
Luminosity ($L_\odot$)	0.77 ± 0.01	0.52 ± 0.01
M_{bol}	5.04 ± 0.02	5.46 ± 0.02
Log (g)	4.46 ± 0.02	4.44 ± 0.02

Table 15. Fundamental stellar parameters for V958 Mon using the mean photometric mass ratio ($q_{ptm} = m_2 / m_1$) from the Roche model fits of LC data (2018) and the estimated mass based on empirically derived M-PRs for W UMa type variable stars.

Parameter	*Primary*	*Secondary*
Mass ($M_\odot$)	1.03 0 ± 0.02	0.45 ± 0.01
Radius ($R_\odot$)	0.97 ± 0.01	0.66 ± 0.01
a ($R_\odot$)	2.14 ± 0.01	2.14 ± 0.01
Luminosity ($L_\odot$)	0.64 ± 0.01	0.36 ± 0.01
M_{bol}	5.23 ± 0.01	5.85 ± 0.01
Log (g)	4.48 ± 0.01	4.45 ± 0.01

Table 16. Fundamental stellar parameters for V1309 Her using the mean photometric mass ratio ($q_{ptm} = m_2 / m_1$) from the Roche model fits of LC data (2018) and the estimated mass based on empirically derived M-PRs for W UMa type variable stars.

Parameter	*Primary*	*Secondary*
Mass ($M_\odot$)	1.27 ± 0.04	0.27 ± 0.01
Radius ($R_\odot$)	1.29 ± 0.01	0.64 ± 0.01
a ($R_\odot$)	2.50 ± 0.02	2.50 ± 0.02
Luminosity ($L_\odot$)	2.21 ± 0.17	0.59 ± 0.01
M_{bol}	3.89 ± 0.02	5.32 ± 0.02
Log (g)	4.32 ± 0.02	4.26 ± 0.02

axis, solar luminosity, bolometric V-mag, and surface gravity of each component. Three empirically derived mass-period relationships (M-PR) for W UMa binaries have been published. The first M-PR was reported by Qian (2003) while two others followed from Gazeas and Stępień (2008) and then Gazeas (2009). According to Qian (2003) when the primary star is less than 1.35 $M_\odot$ or the system is W-type its mass can be determined from Equation 16:

$$\log(M_1) = 0.391\ (59) \cdot \log(P) + 1.96\ (17), \quad (16)$$

where P is the orbital period in days and leads to $M_1 = 1.10 \pm 0.09\ M_\odot$ for the primary. The M-PR (Equation 17) derived by Gazeas and Stępień (2008):

$$\log(M_1) = 0.755\ (59) \cdot \log(P) + 0.416\ (24), \quad (17)$$

corresponds to an OCB system where $M_1 = 1.21 \pm 0.10\ M_\odot$. Gazeas (2009) reported another empirical relationship (Equation 18) for the more massive (M_1) star of a contact binary such that:

$$\log(M_1) = 0.725\,(59) \cdot \log(P) - 0.076\,(32) \cdot \log(q) + 0.365\,(32). \quad (18)$$

from which $M_1 = 1.18 \pm 0.08\ M_\odot$. The mean of three values ($M_1 = 1.17 \pm 0.05\ M_\odot$) estimated from Equations 16–18 was used for subsequent determinations of M_2, semi-major axis a, volume-radii r_L, and bolometric magnitudes (M_{bol}) using the formal errors calculated by WDWINT56A (Nelson 2009). The secondary mass = $0.51 \pm 0.02\ M_\odot$ and total mass ($1.67 \pm 0.06\ M_\odot$) were determined using the photometric mass ratio ($q_{ptm} = 0.436 \pm 0.001$) from Roche modeling. In general, the size, mass, luminosity, and surface gravity of the more massive binary component of an OCB closely match values obtained from solitary dwarf main-sequence (MS) stars. By comparison, a single MS dwarf star with a mass similar to the secondary (late K-type) would be considerably smaller ($R_\odot \sim 0.57$), cooler ($T_{eff} \sim 4000$ K) and far less luminous ($L_\odot \sim 0.075$). This is consistent with the general finding that a secondary star in an OCB is over-sized and over-luminous for its mass (Webbink 2003) particularly with W-subtype OCBs where extreme mass ratios ($q \ll 1$) can be observed.

The semi-major axis, $a(R_\odot) = 2.54 \pm 0.03$, was calculated from Newton's version (Equation 19) of Kepler's third law where:

$$a^3 = (G \cdot P^2\ (M_1 + M_2)) / (4\pi^2). \quad (19)$$

The effective radius of each Roche lobe (r_L) can be calculated over the entire range of mass ratios ($0 < q < \infty$) according to an expression (Equation 20) derived by Eggleton (1983):

$$r_L = (0.49q^{2/3}) / (0.6q^{2/3} + \ln(1 + q^{1/3})), \quad (20)$$

from which values for r_1 (0.4522 ± 0.0003) and r_2 (0.3098 ± 0.0002) were determined for the primary and secondary stars, respectively. Since the semi-major axis and the volume radii are known, the radii in solar units for both binary components can be calculated where $R_1 = a \cdot r_1 = 1.15 \pm 0.01\ R_\odot$ and $R_2 = a \cdot r_2 = 0.79 \pm 0.01\ R_\odot$.

Luminosity in solar units ($L_\odot$) for the primary (L_1) and secondary stars (L_2) was calculated from the well-known relationship derived from the Stefan-Boltzmann law (Equation 21) where:

$$L_{1,2} = (R_{1,2}/R_\odot)^2\ (T_{1,2}/T_\odot)^4. \quad (21)$$

Assuming that $T_{eff1} = 5980$ K, $T_{eff2} = 6314$ K, and $T_\odot = 5772$ K, then the solar luminosities ($L_\odot$) for the primary and secondary are $L_1 = 1.52 \pm 0.25$ and $L_2 = 0.89 \pm 0.02$, respectively.

The same approach described for EI CMi was used to determine the preliminary stellar attributes for NSVS 3092802 (Table 14), V958 Mon (Table 15), and V1309 Her (Table 16). Similar results for only V958 Mon have been previously published (Michaels 2016) wherein they agreed favorably (±5%) with those derived from this investigation (Table 15).

4. Conclusions

New times of minimum for EI CMi (n=15), NSVS 3092802 (n=26), V958 Mon (n=60), and V1309 Her (n=17) based on multicolor CCD data were determined from LCs acquired at DBO. Additional values extracted from the SuperWASP, NSVS, and ASAS surveys as well as from the AAVSO International Database via the InternationalVariable Star Index are reported herein. These along with other published values led to new linear ephemerides. In each case all eclipse timings produced what appears to be a quadratic relationship suggesting that their respective orbital periods are changing at different but constant rates. The ETD-diagram for V1309 Her proved to be the most complex with underlying sinusoidal-like variations in the eclipse timing residuals. Two equally probable causes for orbital period modulation include a third gravitationally bound low-mass stellar object or the so-called Applegate effect.

The adopted effective temperatures (T_{eff1}) were based on a composite of sources that included values from an assortment of photometric and astrometric surveys, the Gaia DR2 release of stellar characteristics (Andrae *et al.* 2018), and estimates from LAMOST DR5 spectral data (Zhao *et al.* 2012; Rui *et al.* 2019). Each OCB clearly experiences a total eclipse which is evident as a flattened bottom during Min I, a characteristic of W-subtype variables. It follows that photometric mass ratios determined by Roche modeling should prove to be reliable substitutes for mass ratios derived from RV data. Nonetheless, spectroscopic studies (RV and high resolution classification spectra) will be required to unequivocally determine a total mass and spectral class for each system. Consequently, all parameter values and corresponding uncertainties reported herein should be considered preliminary.

5. Acknowledgements

This research has made use of the SIMBAD database operated at Centre de Données astronomiques de Strasbourg, France. In addition, the Northern Sky Variability Survey hosted by the Los Alamos National Laboratory (https://skydot.lanl.

gov/nsvs/nsvs.php), the All Sky Automated Survey Catalogue of Variable Stars (http://www.astrouw.edu.pl/asas/?page=acvs) and the International Variable Star Index (AAVSO) were mined for essential information. This work also presents results from the European Space Agency (ESA) space mission Gaia. Gaia data are being processed by the Gaia Data Processing and Analysis Consortium (DPAC). Funding for the DPAC is provided by national institutions, in particular the institutions participating in the Gaia MultiLateral Agreement (MLA). The Gaia mission website is https://www.cosmos.esa.int/gaia. The Gaia archive website is https://archives.esac.esa.int/gaia. This paper makes use of data from the first public release of the WASP data as provided by the WASP consortium and services at the NASA Exoplanet Archive, which is operated by the California Institute of Technology, under contract with the National Aeronautics and Space Administration under the Exoplanet Exploration Program. The use of public data from LAMOST is also acknowledged. Guoshoujing Telescope (the Large Sky Area Multi-Object Fiber Spectroscopic Telescope LAMOST) is a National Major Scientific Project built by the Chinese Academy of Sciences. Funding for the project has been provided by the National Development and Reform Commission. LAMOST is operated and managed by the National Astronomical Observatories, Chinese Academy of Sciences. Many thanks to the anonymous referee whose valuable commentary led to significant improvement of this paper.

References

Akerlof, C., *et al.* 2000, *Astron. J.*, **119**, 1901.
Almeida, L. A., *et al.* 2015, *Astrophys. J.*, **812**, 102.
Alton, K. B. 2019, *J. Amer. Assoc. Var. Star Obs.*, **47**, 7.
Alton, K. B., and Nelson, R. H. 2018, *Mon. Not. Roy. Astron. Soc.*, **479**, 3197.
Alton, K. B., Nelson, R. H. and Stępień, K. 2020, *J. Astrophys. Astron.*, **41**, 26.
Amôres, E. B., and Lépine. 2005, *Astron. J.*, **130**, 659.
Andrae, R., *et al.* 2018, *Astron. Astrophys.*, **616A**, 8.
Applegate, J. H. 1992, *Astrophys. J.*, **385**, 621.
Arbutina, B. 2009, *Mon. Not. Roy. Astron. Soc.*, **394**, 501.
Bailer-Jones, C. A. L. 2015, *Publ. Astron. Soc. Pacifc*, **127**, 994.
Berdyugina, S. V. 2005, *Living Rev. Solar Phys.*, **2**, 8.
Berry, R., and Burnell, J. 2005, *The Handbook of Astronomical Image Processing*, 2nd ed., Willmann-Bell, Richmond VA.
Binnendijk, L. 1970, *Vistas Astron.*, **12**, 217.
Bradstreet, D. H. 2005, in *The Society for Astronomical Sciences 24th Annual Symposium on Telescope Science*, The Society for Astronomical Sciences, Rancho Cucamonga, CA, 23.
Bradstreet, D. H., and Steelman, D. P. 2004, BINARY MAKER 3, Contact Software (http://www.binarymaker.com).
Butters, O. W., *et al.* 2010, *Astron. Astrophys.*, **520**, L10.
Christiansen, J. L., *et al.* 2008, *Mon. Not. R. Astron. Soc.*, **385**, 1749.
Diethelm, R. 2006, *Inf. Bull. Var. Stars*, No. 5713, 1.
Diethelm, R. 2007, *Inf. Bull. Var. Stars*, No. 5781, 1.
Diethelm, R. 2008, *Inf. Bull. Var. Stars*, No. 5837, 1.
Diethelm, R. 2010, *Inf. Bull. Var. Stars*, No. 5920, 1.
Diethelm, R. 2011, *Inf. Bull. Var. Stars*, No. 5992, 1.
Drake, A. J., *et al.* 2014, *Astrophys. J., Suppl. Ser.*, **213**, 9.
Eggleton, P. P. 1983, *Astrophys. J.*, **268**, 368.
Gazeas, K. D. 2009, *Commun. Asteroseismology*, **159**, 129.
Gazeas, K., and Stępień, K. 2008, *Mon. Not. Roy. Astron. Soc.*, **390**, 1577.
Gettel, S. J., Geske, M. T., and McKay, T. A. 2006, *Astron. J.*, **131**, 621.
Giménez, A., Guinan, E., Niarchos, P., and Rucinski, S., eds. 2006, *Close Binaries in the 21st Century: New Opportunities and Challenges*, Springer, Dordrecht.
Greaves, J., and Wils, P. 2003, *Inf. Bull. Var. Stars*, No. 5458, 1.
Henden, A. A., Levine, S. E., Terrell, D., Smith, T. C., and Welch, D. L. 2011, *Bull. Amer. Astron. Soc.*, **43**.
Henden, A. A., and Stone, R. C. 1998, *Astron. J.*, **115**, 296.
Henden, A. A., Terrell, D., Welch, D., and Smith, T. C. 2010, *Bull. Amer. Astron. Soc.*, **42**, 515.
Henden, A. A., Welch, D. L., Terrell, D., and Levine, S. E. 2009, *Bull. Amer. Astron. Soc*., **41**, 669.
Hoffman, D. I., Harrison, T. E., and McNamara, B. J. 2009, *Astron. J.*, **138**, 466.
Houdashelt, M. L., Bell, R. A., and Sweigart, A. V. 2000, *Astron. J.*, **119**, 1448.
Hübscher, J. 2014, *Inf. Bull. Var. Stars*, No. 6118, 1.
Hübscher, J. 2017, *Inf. Bull. Var. Stars*, No. 6196, 1.
Hübscher, J., and Lehmann, P. B. 2015, *Inf. Bull. Var. Stars*, No. 6149, 1.
IonDev SRL. 2020, QTIPLOT 0.9.9-rc9 (https://www.qtiplot.com).
Irwin, J. B. 1959, *Astron. J.*, **64**, 149.
Juryšek, J., *et al.* 2017, *Open Eur. J. Var. Stars*, **179**, 1.
Kallrath, J., and Milone, E. F. 1999, *Eclipsing Binary Stars: Modeling and Analysis*, Springer, New York.
Kukarkin, B. V., *et al.* 1970, *General Catalogue of Variable Stars. Volume II*, 3rd. ed., Moscow.
Kurucz, R. L. 2002, *Baltic Astron.*, **11**, 101.
Kwee, K. K., and van Woerden, H. 1956, *Bull. Astron. Inst. Netherlands*, **12**, 327.
Lucy, L. B. 1967, *Z. Astrophys.*, **65**, 89.
Michaels, E. J. 2016, *J. Amer. Assoc. Var. Star Obs.*, **44**, 53.
Minor Planet Observer. 2010, MPO Software Suite (http://www.minorplanetobserver.com), BDW Publishing, Colorado Springs.
Mochnacki, S .W., and Doughty, N. A. 1972, *Mon. Not. Royal Astron. Soc.*, **156**, 51.
Nelson, R. H. 2009, WDWINT56A: Astronomy Software by Bob Nelson (https://www.variablestarssouth.org/bob-nelson).
Nelson, R. H. 2010, *Inf. Bull. Var. Stars*, No. 5929, 1.
Nelson, R. H. 2011, *Inf. Bull. Var. Stars*, No. 5966, 1.
Nelson, R. H. 2012, *Inf. Bull. Var. Stars*, No. 6018, 1.
O'Connell, D. J. K. 1951, *Publ. Riverview Coll. Obs.*, **2**, 85.
Otero, S., Wils, P., and Dubovsky, P. A. 2004, *Inf. Bull. Var. Stars*, No. 5570, 1.
Paczyński, B., Sienkiewicz, R., and Szczygieł, D. M. 2007, *Mon. Not. Roy. Astron. Soc.*, **378**, 961.
Paczyński, B., Szczygieł, D. M., Pilecki, B., and Pojmański, G. 2006, *Mon. Not. Royal Astron. Soc.*, **368**, 1311.
Paschke, A. 2015, *Open Eur. J. Var. Stars*, **172**, 1.
Paschke, A. 2020, *BAV Rundbrief*, **69**, 101.

Paunzen, E., and Vanmunster, T. 2016, *Astron. Nachr.*, **337**, 239.
Pecaut, M., and Mamajek, E. E. 2013, *Astrophys. J., Suppl. Ser.*, **208**, 9.
Pojmański, G., Pilecki, B., and Szczygieł, D. 2005, *Acta Astron.*, **55**, 275.
Pribulla, T., and Ruciński, S. M. 2006, *Astron. J.*, **131**, 2986.
Prša, A., and Zwitter, T. 2005, *Astrophys. J.*, **628**, 426.
Prša, A., *et al.* 2011, *Astron. J.*, 141, 83
Qian, S-B. 2003, *Mon. Not. Roy. Astron. Soc.*, **342**, 1260.
Qian, S., Yang, Y., Zhu, L., H., He, J., and Yuan, J. 2006, *Astrophys. Space Sci.*, **304**, 25.
Ruciński, S. M. 1969, *Acta Astron.*, **19**, 245.
Ruciński, S. M. 1994, *Publ. Astron. Soc. Pacific*, **106**, 462.
Ruciński, S. M. 1997a, *Astron. J.*, **113**, 407.
Ruciński, S. M. 1997b, *Astron. J.*, **113**, 1112.
Rui, W., *et al.* 2019, *Pub. Astron. Soc. Pacifc*, **131**, 024505.
Smith, T. C., Henden, A. A., and Starkey, D. R. 2011, in *The Society for Astronomical Sciences 30th Annual Symposium on Telescope Science*, The Society for Astronomical Sciences, Rancho Cucamonga, CA, 121.
Software Bisque. 2019, TheSkyX professional edition 10.5.0 (http://www.bisque.com).
Sriram, K., Malu, S., Choi, C. S., and Rao, P. 2016, *Astron. J.*, **151**, 69
Stępień, K. 2006, *Acta Astron.*, **56**, 199.
Stępień, K., and Kiraga, M. 2015, *Astron. Astrophys.*, **577A**, 117.
Stępień, K., Schmitt, J. H. M. M., and Voges, W. 2001, *Astron. Astrophys.*, **370**, 157.
Szczygieł, D. M., Socrates, A., Paczyński, B., Pojmański, G., and Pilecki, B. 2008, *Acta Astron.*, **58**, 405.
Terrell, D., and Wilson, R. E. 2005, *Astrophys. Space Sci.*, **296**, 221.
Tian, Y. P., Xiang, F. Y., and Tao, X. 2009, *Astrophys. Space Science*, **319**, 119.
Udalski, A., Szymanski, M., Kaluzny, J., Kubiak, M., and Mateo, M. 1992, *Acta Astron.*, **42**, 253.
van Hamme, W. 1993, *Astron. J.*, **106**, 2096.
van't Veer, F., 1975, *Astron. Astrophys.*, **40**, 167.
Voges, W., *et al.* 1999, *Astron. Astrophys.*, **349**, 389.
Völschow, M., Schleicher, D. R. G., Perdelwitz, V., and Banerjee, R. 2016, *Astron. Astrophys.*, **587**, 34.
Warner, B. D. 2007, *Minor Planet Bull.*, **34**, 113.
Watson, C., Henden, A. A., and Price, C. A. 2014, AAVSO International Variable Star Index VSX (Watson+, 2006–2014; http://www.aavso.org/vsx).
Webbink, R. F. 2003, in *3D Stellar Evolution*, ASP Conf. Proc. 293, 76.
Wilson, R. E. 1979, *Astrophys. J.*, **234**, 1054.
Wilson, R. E. 1990, *Astrophys. J.*, **356**, 613.
Wilson, R. E., and Devinney, E. J. 1971, *Astrophys. J.*, **166**, 605.
Woźniak, P. R., *et al.* 2004, *Astrophys. J.*, **127**, 2436.
Wright, N. J., Drake, J. J., Mamajek, E. E., and Henry, G. W. 2011, *Astrophys. J.*, **743**, 48.
Zasche, P., Liakos, A., Niarchos, P., Wolf, M., Manimanis, V., and Gazeas, K. 2009, *New Astron.*, **14**, 121.
Zhao, G., Zhao, Y.-H., Chu, Y.-Q., Jing, Y.-P., and Deng, L.-C. 2012, *Res. Astron. Astrophys.*, **12**, 723.